Journal of Sound and Vibration 329 (2010) 4017–4039

Contents lists available at ScienceDirect

Journal of Sound and Vibration

journal homepage: www.elsevier.com/locate/jsvi

Bifurcation analysis on the hunting behavior of a dual-bogie railway vehicle using the method of multiple scales

Pilkee Kim, Jongwon Seok *

School of Mechanical Engineering, College of Engineering, Chung-Ang University, 221 HeukSeok-Dong, DongJak-Gu, Seoul 156-756, Republic of Korea

ARTICLE INFO

Article history:
Received 23 October 2009
Received in revised form
31 January 2010
Accepted 20 March 2010
Handling Editor: L.G. Tham

ABSTRACT

A bifurcation analysis is performed on a nonlinear railway vehicle having dual-bogies to examine the coupling effect of the bogies on the vehicle's hunting behavior. Because of the coupled nature of these bogies, a pair of complex conjugate roots exists in the linearized system close to the origin in addition to the most dominant pair of roots at the hunting speed. Using these four principal modes and a scaling parameter introduced in a novel way, the original systems of equations are converted into new equations whose linear portions exhibit monofrequency oscillations. The solutions near the hunting speed are constructed with an asymptotic expansion of a small perturbation parameter using the method of multiple scales.

Steady state solutions are sought near the hunting speed and the corresponding limit cycle behavior is investigated. The stability of these limit cycles is characterized using Lyapunov's indirect method for the steady state solutions, which is also a novel approach. To support the stability results validity, a series of numerical simulations are performed. Bifurcation diagrams for the lateral motion of the vehicle system are then obtained, and the effects of nonlinearity on the vehicle's hunting behavior are thoroughly examined.

1. Introduction

In the past few decades, the hunting characteristics above the critical speed of a railway vehicle system have been regarded as one of the most important issues concerning the stability of the system. However, previous studies have been mainly focused on simple systems composed of wheelsets and bogie frames, and the methodologies used to analyze the system stability and the associated dynamic behavior are mostly based on rough indirect methods and numerical simulations of the linearized alternatives of the nonlinear systems [1–6].

The railway vehicle system generally includes various nonlinearities such as the flange contact, dry friction, nonlinear dynamic elements, and nonlinear creeps (with their saturation effect) that occur at the contacting interfaces between the rail and the wheels. Even though these nonlinear factors complicate the underlying problem, they are significant and should be considered when analyzing the system stability.

In the special case where a vehicle runs on a straight rail without a distinctively large disturbance, the stability analysis using Lyapunov's indirect method may yield a correct measure of the system stability. However, when perturbations on the vehicle states are large compared to the equilibrium states, the stability results significantly deviate from those obtained using Lyapunov's indirect method [7]. For a nonlinear dynamic system, such as a railway vehicle, it is known that the system parameters or initial conditions could generate multiple solutions. This phenomenon is known as 'bifurcation' [8].

* Corresponding author. Tel.: +82 2 820 5729; fax: +82 2 3280 9982.
E-mail address: seokj@cau.ac.kr (J. Seok).

0022-460X/$ - see front matter © 2010 Elsevier Ltd. All rights reserved.
doi:10.1016/j.jsv.2010.03.024

Nomenclature

a half of the track gauge
a_q amplitude of ξ_q
A_{kq} (k,q)th component of Jacobian matrix evaluated at the equilibrium point
b_{c1}, b_{c3} half of the secondary longitudinal and vertical spring arms
b_{c2}, b_{c4} half of the secondary longitudinal and vertical damper arms
b_{t1}, b_{t3} half of the primary longitudinal and vertical spring arms
b_{t2}, b_{t4} half of the primary longitudinal and vertical damper arms
$C_p^{(n)}$ arbitrary constants to be determined for $\xi_p^{(n)}$
C_{px}, C_{py}, C_{pz} primary longitudinal, lateral, and vertical damping coefficients, respectively
C_{sx}, C_{sy}, C_{sz} secondary longitudinal, lateral, and vertical damping coefficients, respectively
f_{11}, f_{12}, f_{22}, f_{33} lateral, lateral/spin, spin, and longitudinal creep coefficients, respectively
f_k nonlinear forcing terms that include the flange contact and the heuristic creep forces
F_{Lxij}, F_{Lyij}, F_{Lzij} linear creep force of the left wheel in the longitudinal, lateral, and vertical direction, respectively
F^*_{Lxij}, F^*_{Lyij} linear creep force of the left wheel in the longitudinal and lateral direction given by the Kalker's linear theory
$F_p^{(n)}$ nth order function of the pth forcing term
F_{Rxij}, F_{Ryij}, F_{Rzij} linear creep force of the right wheel in the longitudinal, lateral, and vertical direction, respectively
F^*_{Rxij}, F^*_{Ryij} linear creep force of the right wheel in the longitudinal and lateral direction given by the Kalker's linear theory
F_{syc}, F_{syti}, F_{sywij} suspension forces of the carbody, bogies, and wheelsets, respectively, in the lateral direction
F_{szc}, F_{szti}, F_{szwij} suspension forces of the carbody, bogies, and wheelsets, respectively, in the vertical direction
F_{tij} flange contact force
g gravitational acceleration
h height of the vehicle body mass center above the wheelset mass center
h_0 height of the secondary suspension above the bogie frame mass center
h_G height of the bogie mass center above the wheelset mass center
I_{cx}, I_{cy}, I_{cz} roll, pitch, and yaw moments of inertia of the vehicle body, respectively
I_{tx}, I_{ty}, I_{tz} roll, pitch, and yaw moments of inertia of the bogie frame, respectively
I_{wx}, I_{wy}, I_{wz} roll, pitch, and yaw moments of inertia of the wheelset, respectively
K_{px}, K_{py}, K_{pz} primary longitudinal, lateral, and vertical stiffnesses, respectively
K_{ry}, K_{rz} vertical and lateral rail stiffnesses
K_{sx}, K_{sy}, K_{sz} secondary longitudinal, lateral, and vertical stiffnesses, respectively
L_c distance between the vehicle body and the bogie frame mass centers
L_{t1}, L_{t2} half of the primary lateral spring and damper arms
m_c, m_t, m_w vehicle body, bogie frame, and wheelset masses, respectively
M_{Lxij}, M_{Lzij} linear creep moment of the left wheel in the longitudinal and vertical direction
M^*_{Lzij} linear creep moment of the left wheel in the vertical direction given by the Kalker's linear theory
M_{Rxij}, M_{Rzij} linear creep moment of the right wheel in the longitudinal and vertical direction
M^*_{Rzij} linear creep moment of the right wheel in the vertical direction given by the Kalker's linear theory
M_{sxc}, M_{sxti}, M_{sxwij} suspension moments of the carbody, bogies, and wheelsets, respectively, in the longitudinal direction
M_{syc}, M_{syti}, M_{sywij} suspension moments of the carbody, bogies, and wheelsets, respectively, in the lateral direction
M_{szc}, M_{szti}, M_{szwij} suspension moments of the carbody, bogies, and wheelsets, respectively, in the vertical direction
N_{Lyij}, N_{Lzij} normal forces on the left wheel in the lateral and vertical directions
N_{Ryij}, N_{Rzij} normal forces on the right wheel in the lateral and vertical directions
r_0 nominal wheelset rolling radius
r_L, r_R left- and right-wheel rolling radii
R_{Lxij}, R_{Lyij}, R_{Lzij} x, y, z components of the contact position vector on the left wheel, respectively
R_{Rxij}, R_{Ryij}, R_{Rzij} x, y, z components of the contact position vector on the right wheel, respectively
R_y radius of the curved track
T_n time scale of the nth order
V forward speed of the vehicle
x_k kth state variable
y_c, z_c, ψ_c, ϕ_c, γ_c lateral, vertical displacements, and yaw, roll, pitch angles of the carbody, respectively
y_{ti}, z_{ti}, ψ_{ti}, ϕ_{ti}, γ_{ti} lateral, vertical displacements, and yaw, roll, pitch angles of the bogies, respectively
y_{wij}, z_{wij}, ψ_{wij}, ϕ_{wij} lateral, vertical displacements, and yaw, roll angles of the wheelsets, respectively

Greek symbols

α_{ij} saturation constant of heuristic creep model
β_{ij} nonlinearity of heuristic creep model
β_{Lij} nonlinearity of heuristic creep model of the left wheel
β_{Rij} nonlinearity of heuristic creep model of the right wheel
δ flange clearance
δ_{ij} Kronecker delta function

δ_L, δ_R	contact angle of the left and right wheels
ε	a small perturbation parameter
ε^*	a small negative real number
$\zeta_p^{(m)}$	mth complex Fourier coefficient of $F_p^{(2)}$
$\eta_p^{(1)}$	1st complex Fourier coefficients of $F_p^{(3)}$
θ_q	phase angle of ξ_q
$\hat{\theta}$	a phase difference ($=\theta_1-\theta_2$)
ϕ_{se}	cant angle of rail
$\Phi_p^{(m)}$	mth complex Fourier coefficient of $F_p^{(1)}$
$\varphi_k^{(q)}$	kth component of qth eigenvector
$\chi_k^{(j)}$	kth component of the adjoint eigenvector associated with eigenvalue λ_j
κ	a scaling parameter
κ^*	complex conjugate of κ
λ	wheel conicity
λ_i	ith eigenvalue
λ_p^{κ}	0,0,i$\omega\kappa$,$-$i$\omega\kappa$* for p=1,2,3,4
μ	coefficient of friction
ξ_q	qth modal coordinate
$\xi_p^{(n)}$	nth order periodic function of different time scales T_0,T_1,T_3,…, on the pth modal coordinate
ω	Hopf bifurcation frequency (rad/s)
ω'	an angular frequency very close to the Hopf bifurcation frequency (rad/s)

Subscripts

i	location of bogies: i=1 (front bogie), i=2 (rear bogie)
j	location of wheelsets: j=1 (leading wheelset), j=2 (trailing wheelset)

In a study performed by Huilgol [9], the Hopf bifurcation of a wheelset system incorporating nonlinear wheel/rail contact forces was analyzed. To overcome the limitations of linear approximation methods in stability analysis, Moelle et al. [10] and Gasch et al. [11] performed bifurcation analyses for nonlinear single-bogie vehicle systems.

To describe the bifurcation characteristics of a dual-bogie vehicle system, True et al. [12–15] took into account the nonlinear creep forces and their saturation effects. The results show the existence of subcritical Hopf bifurcation that bifurcates from the hunting speed and the possible existence of multiple critical speeds in nonlinear systems. To describe the periodic, quasiperiodic, and chaotic motions of a simplified wheelset model under the nonlinear friction laws of rolling, Knudsen et al. [16] used the Poincare section and map. Ahmadian and Yang [17,18] performed a bifurcation analysis on a nonlinear system having wheelset and bogie systems with nonlinear yaw damping and flange contact. Their analysis is a mathematical improvement from the earlier work of True et al. [12–15].

The studies cited above were mostly confined to the small degrees of freedom (DOF) of the target systems, which simply included the wheelset and the bogie frame. Therefore, to more accurately account for the coupling effects between various components, a full vehicle model is required. Chung et al. [19] performed a bifurcation analysis on a full vehicle model, albeit with a limited 17 DOF, by treating the nonlinear relationships as a two-point boundary value problem. To support the validity of their results regarding the critical speed of a nonlinear vehicle system, Chung et al. [20] compared the bifurcation modeling results with experimental data attained using a full-scale roller rig. Zeng et al. [21] also performed a bifurcation analysis on a 17 DOF vehicle system that included a coupler traction force. They used a Poincare map to obtain the limit cycle behavior and compared the bifurcation results for straight and curved tracks. The full vehicle bifurcation diagrams of Refs. [19–21] still exhibit single branches similar to those of single-bogie vehicle systems, and the bifurcation characteristics due to the coupling between the two bogies could not be explained.

In a set of differential equations used to describe a vehicle's dynamic behavior, when the contribution of nonlinear terms is small compared to the contribution of linear terms, a variety of perturbation methods are known to be effective at solving the dynamic problem with sufficient accuracy [22]. Among these techniques, the method of asymptotic expansion proposed by Bogoliubov et al. [23] may provide the most adequate approach to solve oscillating, multi-degree of freedom, weakly nonlinear systems in the presence of internal friction. In such circumstances, the system appears to undergo near-monofrequency oscillations because high-frequency oscillating components tend to be damped out rapidly. Ahmadian and Yang [17,18] employed this method to calculate the limit cycles of a nonlinear vehicle system through an expansion of the running speed in the vicinity of the hunting speed, and added the first-order solution to the linear terms. While an improvement of the linear solution, this approach will still provide less accurate results for a system with higher order nonlinearities. Additionally, the proposed method is limited to monofrequency oscillations, and thus not adequate for a system with multiple critical eigenvalues.

The railway vehicle generally includes dual-bogies having identical dynamic characteristics. It is known that such a system has mode interaction due to the existence of several pairs of eigenvalues, which are very close in values [24]. Through the inspection of the root locus diagram, it can be easily observed that several root loci entail their shadowed ones. For the railway vehicle under consideration, these eigenvalues are caused by the coupling effects of the two identical bogie systems that are weakly connected to the vehicle body. Additionally, the most dominant roots entail their shadowed ones. Thus, an improved approach considering multiple critical eigenvalues is needed to investigate the hunting motion of a dual-bogie railway vehicle system.

In this study, the target system is a 31-DOF full railway vehicle model with its flange contact and heuristic creeps. The resulting system equations for the dual-bogie railway vehicle yield two sets of principal conjugate roots, one corresponding to the most dominant principal eigenmodes and the other associated with its shadowed eigenmodes.

Because the resulting multifrequency oscillations hinder the application of the asymptotic approximation procedure, a scaling parameter is introduced. This parameter and the biorthogonality relationships allows us to model the multifrequency (but close to monofrequency) oscillating system like one that has monofrequency oscillations. Using the method of multiple scales, the asymptotic approximations of the modal coordinates are obtained as functions of the amplitudes and phase angles that can be represented by mutually coupled first order differential equations (i.e. modulation equations).

To investigate the bifurcation characteristics of the vehicle system under consideration, the limit cycles are obtained, and the stability of the resulting limit cycles is examined. It is worth nothing that the stability of the vehicle system considered in this study is not a sole function of an amplitude as treated in Refs. [17,18] but a function of two amplitudes and their phase difference. Accordingly, Lyapunov's indirect method is applied to the modulation equations in order to determine the stability of the limit cycle. Also, it should be noted that the use of Lyapunov's indirect method to determine stability is completely different from the conventional use of this method to determine the hunting speed by directly applying the eigenanalysis to the linearized system [1–6].

To verify the effectiveness of the proposed asymptotic approximation procedure, first, second, and third approximations are computed semi-analytically using the symbolic language Maple^{TM} [25]. Results are then compared to those obtained by direct numerical integration. The bifurcation analysis for the system with linear creep is performed separately from the system with heuristic creep, and their results compared and discussed.

2. Equations of motion for the 31-DOF vehicle system

Fig. 1 is a schematic of the railway vehicle system, where stiffness and damping elements have been incorporated into the suspensions. As shown in Fig. 1, the model system includes a vehicle body, front and rear bogies positioned with mirror symmetry relative to a midplane, and two identical wheelsets for each bogie frame. All possible motions (lateral, vertical, yawing, rolling, and pitching) of the system components (vehicle body, bogie frames, and wheelsets) are coupled through the primary and secondary suspensions. It should be noted that there is no pitching motion of wheelset. The result is a system with a total of 31 DOF (5 DOF for the vehicle body, 5 DOF for each of the two bogies, and 4 DOF for each of the four wheelsets).

The dynamic behavior and stability are partially governed by the contact mechanisms between the wheel and rail surfaces, whose schematics are shown in Fig. 2(a). These contacts can generally be classified into two categories, the primary contacts which occur at the interfacial surface and induce non-conservative creep forces in the elliptical contact region, and the secondary contacts which impact the rail side when the clearance between the wheel flange and the rail becomes zero. In this study, a heuristic creep theory is employed to account for the nonlinear creep phenomenon that occurs due to the saturation effect of the adhesion limit. It is assumed that the wheel is conical and the rail knife-edged in shape with known lateral and vertical stiffnesses [26], as shown in Fig. 2(b). Based on this wheel-rail configuration, the flange contact force can be considered to be a spring reaction force restricted by a dead-band.

The equations of motion for the vehicle system can be derived [6], with the appropriate linear and angular displacements, based on the Cartesian coordinate systems shown in Fig. 1. Using some linearization and simplification procedures, the equations of motion for the vehicle body and the bogie frames in the lateral, vertical, yaw, roll, and pitch

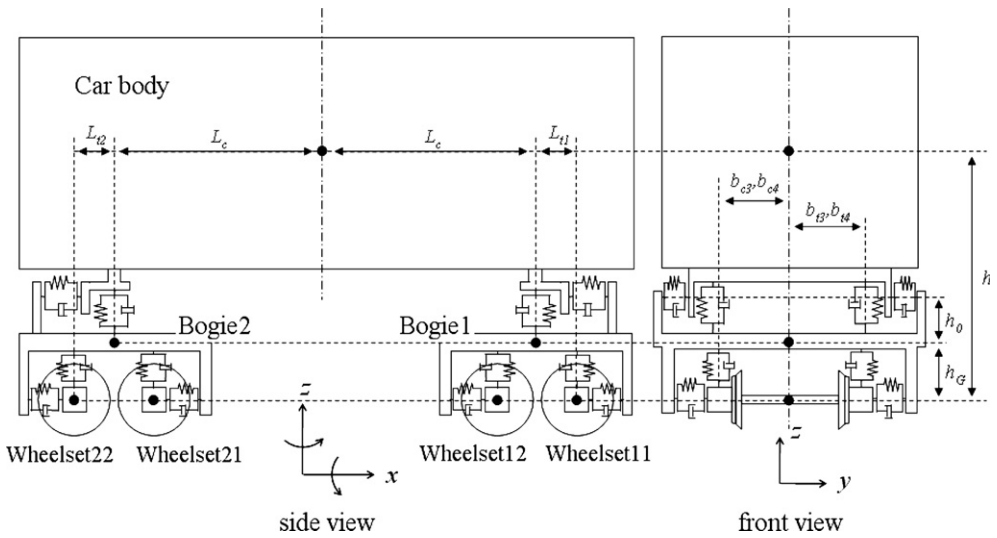

Fig. 1. A schematic of the vehicle system.

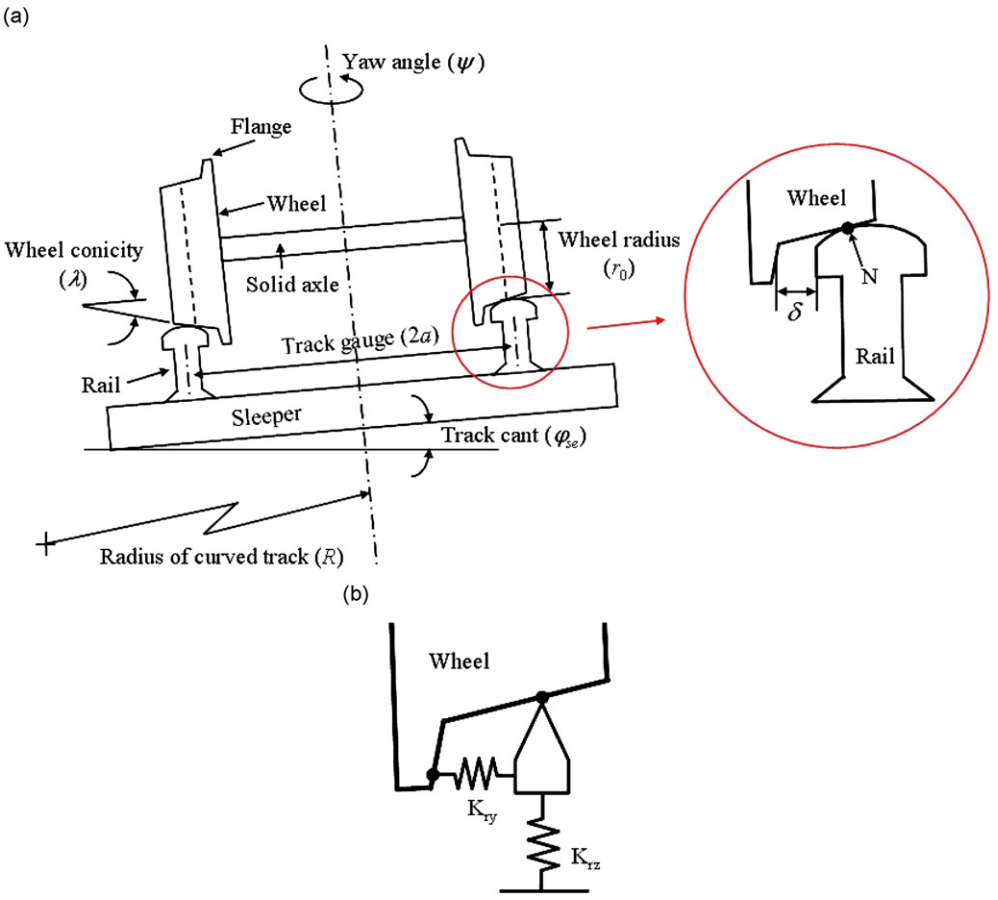

Fig. 2. (a) A schematic of the wheel–rail contact mechanism and (b) its dynamic model.

directions are obtained, respectively, in the form

$$m_q\left(\ddot{y}_q-\frac{V^2}{R_y}\right)=-m_q g\phi_{se}+F_{syq},(q=c,t1,t2), \tag{1a}$$

$$m_q\left(\ddot{z}_q+\frac{V^2\phi_{se}}{R_y}\right)=-m_q g+F_{szq},(q=c,t1,t2), \tag{1b}$$

$$I_{qz}\ddot{\psi}_q=M_{szq},(q=c,t1,t2), \tag{1c}$$

$$I_{qx}\ddot{\phi}_q=M_{sxq},(q=c,t1,t2), \tag{1d}$$

$$I_{qy}\ddot{\gamma}_q=M_{syq},(q=c,t1,t2), \tag{1e}$$

where c, $t1$, and $t2$ for the subscript q represent the vehicle body, the front bogie frame, and the rear bogie frame, respectively. F_{syq}, F_{szq}, M_{sxq}, M_{syq}, M_{szq} represent the suspension forces in the lateral and vertical directions and the suspension moments in the roll, pitch, and yaw directions, respectively. To avoid a lengthy description, the details of these suspension forces/moments are given in Appendix A and the associated physical parameters are defined in the nomenclature.

Similarly, the equations of motion for the wheelsets in the lateral, vertical, yaw, and roll directions are, respectively, given by

$$m_w\left(\ddot{y}_{wij}-\frac{V^2}{R_y}\right)=-m_w g\phi_{se}+(\alpha_{ij}F_{Lyij}+\alpha_{ij}F_{Ryij})+N_{Lyij}+N_{Ryij}+F_{sywij}-F_{tij}, \tag{2a}$$

$$m_w\left(\ddot{z}_{wij}+\frac{V^2\phi_{se}}{R_y}\right)=-m_w g+(F_{Lzij}+F_{Rzij})+N_{Rzij}+N_{Lzij}+F_{szwij}, \tag{2b}$$

$$I_{wz}\ddot{\psi}_{wij}+\frac{I_{wy}V\dot{\phi}_{wij}}{r_0}=R_{Rxij}\alpha_{ij}F_{Ryij}-R_{Ryij}\alpha_{ij}F_{Rxij}+R_{Lxij}\alpha_{ij}F_{Lyij}-R_{Lyij}\alpha_{ij}F_{Lxij}+R_{Rxij}N_{Ryij}+R_{Lxij}N_{Lyij}+\alpha_{ij}M_{Lzij}+\alpha_{ij}M_{Rzij}+M_{szwij}, \tag{2c}$$

$$I_{wx}\ddot{\phi}_{wij}+\frac{I_{wy}V\left(\frac{V}{R_y}-\dot{\psi}_{wij}\right)}{r_0}=R_{Ryij}F_{Rzij}-R_{Rzij}\alpha_{ij}F_{Ryij}+R_{Lyij}F_{Lzij}-R_{Lzij}\alpha_{ij}F_{Lyij}+R_{Lyij}N_{Lzij}+R_{Ryij}N_{Rzij}-R_{Rzij}N_{Ryij}-R_{Lzij}N_{Lyij}+M_{Lxij}+M_{Rxij}+M_{sxwij}, \tag{2d}$$

where the subscripts i (i=1 for the front bogie, 2 for the rear bogie) and j (j=1 for the leading wheelset, 2 for the trailing wheelset) represent the location of the wheelset in the vehicle system, the subscripts L and R denote the left- and right-hand sides, respectively. Here, F_{tij} is the flange contact force, and F_{sywij}, F_{szwij}, M_{sxwij}, and M_{szwij} denote the suspension forces in lateral and vertical directions and the suspension moments in the roll and yaw directions, respectively. Also, F_{Lxij}, F_{Lyij}, F_{Lzij}, F_{Rxij}, F_{Ryij}, F_{Rzij}, M_{Lxij}, M_{Lzij}, M_{Rxij}, and M_{Rzij} are the linear creep forces and moments given by the Kalker's linear theory [27]. It should be noted that the saturation constants α_{ij} are multiplied by these linear creep forces to account for a heuristic creep phenomenon. The details of all the reaction forces/moments and the associated physical quantities are given in Appendix A and the nomenclature.

3. Development of nonlinear system equations for asymptotic expansions

As shown in the previous section, the dynamic equations of motion are inherently nonlinear, which prevents us from directly applying a variety of commonly used linear theories. To investigate the hunting behavior of the model system, we first derive the asymptotic solutions of a full railway vehicle system having a total of 31 DOF.

The equations of motion represented in Eqs. (1a)–(1e) and (2a)–(2d) can be expressed in the following index form

$$\frac{dx_k}{dt}=F_k(x_1,\ldots,x_{62}),k=1,\ldots,62, \tag{3}$$

where x_k denote the state variables composed of the displacements and velocities of the system components. Expressing the states of the vehicle system by the sum of the constant equilibrium states, $\bar{x}_k$, and the additional perturbation terms, $\tilde{x}_k$, and expanding the right-hand side of Eq. (3) in a Taylor series at the equilibrium point, Eq. (3) can be transformed into

$$\frac{d\tilde{x}_k}{dt}-\sum_{q=1}^{62}A_{kq}\tilde{x}_q=f_k(\tilde{x}_1,\ldots,\tilde{x}_{62}),k=1,\ldots,62, \tag{4}$$

where A_{kq} are the components of the Jacobian matrix evaluated at the equilibrium point. Note that the functions f_k in Eq. (4) are nonlinear forcing terms that include the flange contact and the heuristic creep forces at the wheel/rail contact interfaces.

The perturbed state variables can be expressed by linear combinations of the weighted eigenvectors in the form

$$\tilde{x}_k=\sum_{q=1}^{62}\xi_q\varphi_k^{(q)},k=1,\ldots,62, \tag{5}$$

where the ξ_q and $\varphi_k^{(q)}$ terms are the qth modal coordinate and the kth component of the associated eigenvector, respectively.

As previously mentioned, due to the coupling effect of the two identical bogies through the vehicle body, the hunting motion of the full vehicle system is mainly governed by the two most dominant conjugate principal eigenvectors and the two associated shadowed ones. This coupling effect is primarily due to two factors, namely the vehicle body high degree of inertia compared to the other elements, and the smallness of the stiffnesses of the secondary suspension compared to those of the primary suspension. Therefore, the two identical bogie systems can be lightly coupled through the vehicle body, and the two pairs of principal roots tend to be located very closely to each other in the complex pole plane. Hence, four principal eigenvectors can be found near the hunting speed. It should be noted that, because of the existence of these shadow principal roots for the dominant principal roots, the limit cycles at the hunting speed do not exhibit monofrequency oscillations which typically appear in the analyses for a single wheelset and single-bogie railway vehicle models [17,18].

In order to represent the perturbed state variables in the vicinity of the hunting speed, we use the four principal eigenvectors under the following assumptions: the system is vibrating with a monofrequency (close to Hopf bifurcation frequency) but with a slowly varying amplitude and phase, and the effects of the other remnant modes are small enough to be neglected. Therefore, the perturbed state variables shown in Eq. (5) can be expressed in the following reduced form:

$$\tilde{x}_k=\sum_{p=1}^{4}\xi_p\varphi_k^{(p)},k=1,\ldots,62. \tag{6}$$

Since the damping of the system under consideration is assumed to be of the viscous type, the autonomous set of state equations is non-self-adjoint [28]. It should be noted that the orthogonal relationships between the eigenvectors are no

more valid in the non-self-adjoint system. In such a system, the solution procedure can be obtained by using the biorthogonality relationships of the eigenvectors of the original system with those of its adjoint system. The biorthogonal relationships are given by [28]

$$\sum_k \chi_k^{(j)} \varphi_k^{(i)} = \delta_{ij}, i,j = 1,2,\ldots,62, \tag{7}$$

$$\sum_{k,l} \chi_k^{(j)} A_{kl} \varphi_l^{(i)} = \lambda_i \delta_{ij}, i,j = 1,2,\ldots,62, \tag{8}$$

where λ_i is the ith eigenvalue, δ_{ij} is the Kronecker delta function, and $\chi_k^{(j)}$ is the kth component of the adjoint eigenvector associated with eigenvalue λ_j.

Substituting Eq. (6) into (4) and introducing the biorthogonal relationships, the differential equations of the modal coordinates are derived in the following reduced form:

$$\frac{d\xi_p}{dt} - \lambda_p \xi_p = f_p', p = 1,\ldots,4, \tag{9}$$

where

$$\lambda_p = \pm i\omega \quad \text{for } p = 1,2, \quad \lambda_p = \varepsilon^* \pm i\omega' \quad \text{for } p = 3,4, \tag{10}$$

$$f_p' = \sum_{k=1}^{62} \chi_k^{(p)} f_k(x_1,\ldots,x_{62};\xi_1,\ldots,\xi_4), \tag{11}$$

where $i = \sqrt{-1}$, λ_p is the pth principal eigenvalue, and $\chi_k^{(p)}$ is the kth component of the associated adjoint eigenvector. Note that ω in Eq. (10) is the Hopf bifurcation frequency of the homogeneous part of Eq. (4).

In addition, $\varepsilon^* \pm i\omega'$ are the shadowed principal eigenvalues, where ε^* is a negative real number that is small compared to its imaginary counterpart, ω', which is assumed to be very close to ω in this study. As indicated in Eq. (10), the full vehicle system under consideration can be described by the two most dominant conjugate principal eigenvalues along with the two conjugate shadowed ones. Consequently, the system has two dominant oscillating frequencies, ω and ω', with a small difference existing between them.

The asymptotic solutions of a nonlinear equation, such as Eq. (9), can be obtained through a variety of perturbation methods [22]. The asymptotic approximation appropriately models the original nonlinear system exhibiting oscillations. The asymptotic solutions are represented as sums of the periodic functions expanded into a power series of a small perturbation parameter (ε). By applying these asymptotic solutions to Eq. (9), the differential equation for each order of the perturbation parameter can be obtained. To satisfy the solvability conditions from which the relevant modulation equations are derived, the secular terms that are included in the forcing terms must be removed. Consequently, the asymptotic solutions of Eq. (9) can be represented as periodic functions with the arguments governed by the corresponding modulation equations.

The forcing terms f_k in Eq. (11) include complicated nonlinear functions that take account of the heuristic creep and flange contact behaviors, making it almost impossible to represent the solvability conditions in closed form. One of the methods that can be applied to circumvent such a difficulty is to expand the forcing terms into Fourier series. Unfortunately, since Eq. (9) is composed of two pairs of mutually conjugate differential equations ($\lambda_p = \pm i\omega$ for p=1, 2 and $\varepsilon^* \pm i\omega'$ for p=3, 4) and is not in the form of a monofrequency oscillation, Fourier coefficients of forcing terms of these equations cannot be derived without modification. However, in the current case the two dominant oscillating frequencies are very close. Hence, the problem at hand can be resolved if a scaling parameter κ is introduced, thus allowing us to express the homogeneous parts of the second pair of Eq. (9) (i.e., for p=3, 4) as identical to the homogeneous parts of the first pair (i.e., for p=1, 2). Eq. (9) can then be reformulated in the form:

$$\frac{d\xi_p}{dt} - \lambda_p' \xi_p = \varepsilon F_p, \text{for } p = 1,\ldots,4, \tag{12}$$

where

$$\lambda_p' = \pm i\omega \text{for } p = 1,2 \text{ or } p = 3,4, \tag{13}$$

$$F_p = f_p' + \lambda_p^{\kappa} \xi_p \tag{14}$$

and ε is a small dimensionless parameter that indicates the weakness of the nonlinear terms when compared to the linear term ($\lambda_p' \xi_p$). In Eq. (14), λ_p^k for p=1,2,3,4 are, respectively, $0, 0, i\omega, \kappa, -i\omega\kappa^*$. Also, $\kappa = \lambda_3/\lambda_1 - 1$ and κ^* is the complex conjugate of κ.

Generally, when perturbation is absent, i.e. ε=0 in Eq. (12), the oscillations will be purely harmonic with a uniform amplitude and phase. On the other hand, the existence of nonlinear perturbations, i.e. $\varepsilon \neq 0$, inevitably results in the additional appearance of overtones in the solutions of Eq. (12). These overtones indicate the dependence between instantaneous frequencies and amplitudes, and they also include information on the increasing or decreasing

characteristics of the oscillation amplitudes, which depend on whether energy is expelled or absorbed by the perturbing forces [23].

4. Asymptotic solutions for the system equations using the method of multiple scales

For asymptotic expansion with small perturbations, use of the derivative expansion method (called the many-variable version of the method of multiple scales [22]) allows us to introduce different time scales, T_n, and time derivatives, d/dt, defined by

$$T_n = \varepsilon^n t, \tag{15}$$

$$\frac{\mathrm{d}}{\mathrm{d}t} = D_0 + \varepsilon D_1 + \varepsilon^2 D_2 + \ldots, \; D_n = \frac{\partial}{\partial T_n}. \tag{16}$$

This method also allows for asymptotic expansions of the modal coordinates in the power of ε

$$\xi_p = \xi_p^{(0)}(T_0,T_1,\ldots) + \varepsilon\xi_p^{(1)}(T_0,T_1,\ldots) + \varepsilon^2\xi_p^{(2)}(T_0,T_1,\ldots) + \cdots, \tag{17}$$

where $\xi_p^{(n)}$ ($p = 1,2,3,4$) is the nth order periodic function of different time scales $T_0,T_1,T_3,\ldots$, on the pth modal coordinate. By substituting Eqs. (16) and (17) into Eq. (12), expanding the right-hand side of Eq. (12) with the lowest periodic function of ξ_p (i.e. $\xi_p^{(0)}$), and collecting like powers of ε, one obtains differential equations with successive orders of ε in the form

$$\varepsilon^0 : D_0\xi_p^{(0)} - \lambda_p'\xi_p^{(0)} = 0, \tag{18a}$$

$$\varepsilon^1 : D_0\xi_p^{(1)} - \lambda_p'\xi_p^{(1)} = F_p^{(1)} - D_1\xi_p^{(0)}, \tag{18b}$$

$$\varepsilon^2 : D_0\xi_p^{(2)} - \lambda_p'\xi_p^{(2)} = F_p^{(2)} - D_1\xi_p^{(1)} - D_2\xi_p^{(0)}, \tag{18c}$$

$$\varepsilon^3 : D_0\xi_p^{(3)} - \lambda_p'\xi_p^{(3)} = F_p^{(3)} - D_1\xi_p^{(2)} - D_2\xi_p^{(1)} - D_3\xi_p^{(0)}, \tag{18d}$$

$$\vdots$$

where $F_p^{(n)}$ is the nth order function of the pth forcing term such that

$$F_p^{(1)} = F_p(\xi_1^{(0)},\ldots,\xi_4^{(0)}), \tag{19a}$$

$$F_p^{(2)} = \sum_{r=1}^{4}\frac{\partial F_p}{\partial\xi_r}(\xi_1^{(0)},\ldots,\xi_4^{(0)})\xi_r^{(1)}, \tag{19b}$$

$$F_p^{(3)} = \sum_{r=1}^{4}\frac{\partial F_p}{\partial\xi_r}(\xi_1^{(0)},\ldots,\xi_4^{(0)})\xi_r^{(2)} + \frac{1}{2}\sum_{r=1}^{4}\sum_{s=1}^{4}\frac{\partial^2 F_p}{\partial\xi_r\partial\xi_s}(\xi_1^{(0)},\ldots,\xi_4^{(0)})\xi_r^{(1)}\xi_s^{(1)}. \tag{19c}$$

The solutions for the unperturbed modal coordinate systems, which are the solutions of Eq. (18a), are composed of two pairs of complex conjugates and can be defined by

$$\xi_p^{(0)} = A_p\mathrm{e}^{\mathrm{i}b(\omega T_0)} \tag{20}$$

where

$$b = \begin{cases} +1 & \text{for } p = 1,3, \\ -1 & \text{for } p = 2,4, \end{cases} \tag{21a}$$

$$A_p = \begin{cases} \dfrac{1}{2}a_1\mathrm{e}^{\mathrm{i}b\theta_1} & \text{for } p = 1,2, \\ \dfrac{1}{2}a_2\mathrm{e}^{\mathrm{i}b\theta_2} & \text{for } p = 3,4, \end{cases} \tag{21b}$$

and the amplitudes a_1, a_2, and phase angles θ_1, θ_2 of ξ_p are functions of T_1, T_2,… .

Substituting Eq. (20) into (18b) and using the complex Fourier series expansions of the forcing terms, $F_p^{(1)}$, we obtain

$$D_0\xi_p^{(1)} - \lambda_p'\xi_p^{(1)} = \sum_{m=-\infty}^{\infty}\Phi_p^{(m)}\mathrm{e}^{\mathrm{i}m\omega T_0} - D_1(A_p\mathrm{e}^{\mathrm{i}b(\omega T_0)}), \tag{22}$$

where $\Phi_p^{(m)}$ is the mth complex Fourier coefficient of $F_p^{(1)}$ calculated by

$$\Phi_p^{(m)} = \frac{1}{2\pi}\int_0^{2\pi} F_p^{(1)}(\xi_1^{(0)},\ldots,\xi_4^{(0)})\mathrm{e}^{-\mathrm{i}m\omega T_0}\,\mathrm{d}(\omega T_0). \tag{23}$$

To determine the dependence on slow scales, one may investigate the higher-order problem and impose conditions that make the expansion uniform. For simple nonlinear vibration problems, the above process leads us to discard secular and small-divisor terms [22]. In order for $\xi_p^{(1)}/\xi_p^{(0)}$ to be bounded for all T_0, the secular term(s) on the right-hand side of Eq. (22) must be eliminated, which results in

$$\Phi_p^{(b)} - D_1(A_p e^{ib(\omega T_0)}) = 0. \tag{24}$$

After removing the secular term, the resulting form of Eq. (22) and its solutions take on the following form

$$D_0\xi_p^{(1)} - \lambda_p'\xi_p^{(1)} = \sum_{m=-\infty, m\neq b}^{\infty} \Phi_p^{(m)} e^{im\omega T_0}, \tag{25}$$

$$\xi_p^{(1)} = \sum_{m=-\infty, m\neq b}^{\infty} \frac{\Phi_p^{(m)}}{i\omega(m-b)} e^{im\omega T_0} + C_p^{(1)} e^{ib\omega T_0}, \tag{26}$$

where $C_p^{(1)}$ are arbitrary constants to be determined.

The substitution of Eqs. (20) and (26) into Eq. (18c) yields

$$D_0\xi_p^{(2)} - \lambda_p'\xi_p^{(2)} = \sum_{m=-\infty}^{\infty} \left\{ \zeta_p^{(m)} - \frac{D_1\Phi_p^{(m)}}{i\omega(m-b)} \right\} e^{im\omega T_0} + \left\{ \zeta_p^{(1)} - D_1 C_p^{(1)} - D_2(A_p e^{ib(\omega T_0)}) \right\}, \tag{27}$$

where $\zeta_p^{(m)}$ is the mth complex Fourier coefficient of $F_p^{(2)}$ calculated by

$$\zeta_p^{(m)} = \frac{1}{2\pi}\int_0^{2\pi} F_p^{(2)}(\xi_1^{(0)}, \ldots, \xi_4^{(0)}, \xi_1^{(1)}, \ldots, \xi_4^{(1)}) e^{-im\omega T_0}\, d(\omega T_0), \tag{28}$$

For the solutions of Eq. (27) to be bounded, all the secular terms in Eq. (27) must be eliminated such that

$$\zeta_p^{(1)} - D_1 C_p^{(1)} - D_2(A_p e^{ib(\omega T_0)}) = 0, \tag{29}$$

and the solutions of the resulting equation may take the form

$$\xi_p^{(2)} = \sum_{m=-\infty, m\neq b}^{\infty} \left[\frac{\zeta_p^{(m)}}{i\omega(m-b)} - \frac{D_1\Phi_p^{(m)}}{\{i\omega(m-b)\}^2} \right] e^{im\omega T_0} + C_p^{(2)} e^{ib\omega T_0}, \tag{30}$$

where $C_p^{(2)}$ are arbitrary constants to be determined.

Similarly, by using Eqs. (20) and (26), introducing Eq. (30) into (18d), and eliminating the secular term, we obtain

$$\eta_p^{(1)} - D_1 C_p^{(2)} - D_2 C_p^{(1)} - D_3(A_p e^{ib(\omega T_0)}) = 0, p = 1 \ldots 4, \tag{31}$$

where $\eta_p^{(1)}$ are the 1st complex Fourier coefficients of $F_p^{(3)}$ calculated by

$$\eta_p^{(1)} = \frac{1}{2\pi}\int_0^{2\pi} F_p^{(2)}(\xi_1^{(0)}, \ldots, \xi_4^{(0)}, \xi_1^{(1)}, \ldots, \xi_4^{(1)}, \xi_1^{(2)}, \ldots, \xi_4^{(2)}) e^{-i\omega T_0}\, d(\omega T_0). \tag{32}$$

By substituting Eq. (21b) into Eqs. (24), (29), and (31), we obtain the modulation equations of a_1, a_2, θ_1, and θ_2 in successive order. Since the secular terms are mutually complex conjugates for p=1,2 and 3,4, taking the equations only for p=1,3 will yield

$$\frac{da_n}{dt} = \varepsilon D_1 a_n + \varepsilon^2 D_2 a_n + \varepsilon^3 D_3 a_n + \cdots, n = 1,2, \tag{33a}$$

$$\frac{d\theta_n}{dt} = \varepsilon D_1 \theta_n + \varepsilon^2 D_2 \theta_n + \varepsilon^3 D_3 \theta_n + \cdots, n = 1,2, \tag{33b}$$

where

$$D_1 a_n = \mathrm{Re}[2\Phi_{n'}^{(1)} e^{-i\theta_n}], \tag{34a}$$

$$D_2 a_n = \mathrm{Re}[2(\zeta_{n'}^{(1)} - D_1 C_n^{(1)}) e^{-i\theta_n}], \tag{34b}$$

$$D_3 a_n = \mathrm{Re}[2(\eta_{n'}^{(1)} - D_1 C_n^{(2)} - D_2 C_n^{(1)}) e^{-i\theta_n}], \tag{34c}$$

$$D_1 \theta_n = \frac{1}{a_n}\mathrm{Im}[2\Phi_{n'}^{(1)} e^{-i\theta_n}], \tag{34d}$$

$$D_2 \theta_n = \frac{1}{a_n}\mathrm{Im}[2(\zeta_{n'}^{(1)} - D_1 C_n^{(1)}) e^{-i\theta_n}], \tag{34e}$$

$$D_3\theta_n = \frac{1}{a_n}\mathrm{Im}[2(\eta_{n'}^{(1)} - D_1C_n^{(2)} - D_2C_n^{(1)})\mathrm{e}^{-\mathrm{i}\theta_n}]. \tag{34f}$$

In Eqs. (34a)–(34f), Re [ ] and Im [ ] denote the real and imaginary parts of their arguments, respectively, and

$$n' = \begin{cases} 1 & \text{for } n = 1, \\ 3 & \text{for } n = 2. \end{cases} \tag{35}$$

The solutions of the modal coordinates for the kth order asymptotic approximation can be obtained by keeping the terms up to the (k–1)th power of ε in Eq. (17) and kth power of ε in Eqs. (33a) and (33b), respectively. Thus, the solutions and the associated modulation equations for the kth asymptotic approximation can be represented by

$$\xi_p = \sum_{j=1}^{k} \varepsilon^{j-1}\xi_p^{(j-1)}, \tag{36a}$$

$$\frac{\mathrm{d}a_n}{\mathrm{d}t} = \sum_{j=1}^{k} \varepsilon^j D_j a_n, \tag{36b}$$

$$\frac{\mathrm{d}\theta_n}{\mathrm{d}t} = \sum_{j=1}^{k} \varepsilon^j D_j \theta_n. \tag{36c}$$

It should be noted that in Eq. (36a), an appropriate order analysis in ε enables us to adopt the asymptotic solutions expanded up to the (k–1)th power of ε instead of the kth power. For instance, consider the first approximation (k=1) of Eqs. (36a)–(36c). If we let $\overline{D_1a_n}$ and $\overline{D_1\theta_n}$ be the average values of D_1a_n and $D_1\theta_n$ in the interval (0, t), then from Eqs. (36b) and (36c), we obtain

$$\Delta a_n = a_n(t) - a_n(0) \approx \varepsilon t(\overline{D_1a_n}), \tag{37a}$$

$$\Delta\theta_n = \theta_n(t) - \theta_n(0) \approx \varepsilon t(\overline{D_1\theta_n}). \tag{37b}$$

It can be seen that the time t, during which the quantities a_n and θ_n may acquire finite changes, is on the order of $1/\varepsilon$. The first approximations of Eqs. (36b) and (36c) arise from neglecting the terms of order ε^2 and higher. An error of order ε in $\mathrm{d}a_n/\mathrm{d}t$ and $\mathrm{d}\theta_n/\mathrm{d}t$, until time t, leads to an error of order $\varepsilon^2 t$ in the functions a_n and θ_n. Hence, in the time interval during which a_n and θ_n undergo finite changes, errors in these quantities are on the order of ε. Thus, keeping the term $\varepsilon\xi_p^{(1)}(a_n,\theta_n)$ is not necessary for the first approximation of Eq. (36a) because the error of using $\xi_p = \xi_p^{(0)}(a_n,\theta_n)$ is on the same order. By the same token, such an order analysis may still hold for higher order asymptotic approximations ($k > 1$) of Eq. (36a).

5. The limit cycle and its stability determination

The direct application of Lyapunov's indirect method to the original (weakly) nonlinear railway vehicle system through linearization at its static equilibrium states is one of the most well-known processes used to identify the system stability in the vicinity of the system's static equilibrium states [1–6]. However, using only Lyapunov's indirect method to determine the stability of a complex nonlinear system, such as railway vehicles with state-dependent nonlinearities, could lead to inaccurate results. For instance, two different initial states of a railway vehicle can result in periodic steady states that are quite different; each one or both may be far from their static equilibrium states.

A limit cycle, which represents steady state periodic motion, exhibits a closed curve in a phase plane because of its periodicity. In the case where all the adjacent paths approach the limit cycle as $t \to +\infty$, the limit cycle is characterized as *stable* or *attractive*, while in the case where all the adjacent paths approach the limit as $t \to -\infty$, the limit cycle is described as *unstable* or *non-attractive*. In all other cases it is neither stable nor unstable. A bifurcation diagram is a very useful way to examine multiple steady state railway vehicle responses caused by nonlinearities. Such a diagram can be obtained by evaluating the stability of a limit cycle through the variation of a parameter of interest (in this study, lateral displacement).

One of the most representative nonlinear analyses is bifurcation analysis [8], a procedure that is composed of two steps, first finding all the solution branches in the region of interest and secondly determining the stability of all these branches. To investigate the bifurcation characteristics of a full railway vehicle system, including the coupling effects of the two bogies, a set of branches representing limit cycles are obtained. This is accomplished through the use of the asymptotic approximation method and the method of multiple scales, in accordance with the vehicle's running speed.

The nth order periodic functions of the principal modal coordinates $\xi_p^{(n)}$ (p=1,…,4) are functions of a_1, a_2, θ_1, θ_2, and implicitly the time t. At a steady state, the amplitudes of oscillation (a_1, a_2) and the phase difference $\hat{\theta}(=\theta_1-\theta_2)$ must be time-independent and thus, constant. Therefore, to represent a limit cycle, the following equations must be simultaneously satisfied:

$$\frac{\mathrm{d}a_1}{\mathrm{d}t}(a_1,a_2,\theta_1,\theta_2) = 0, \tag{38a}$$

$$\frac{da_2}{dt}(a_1,a_2,\theta_1,\theta_2)=0, \tag{38b}$$

$$\frac{d\hat{\theta}}{dt}=\frac{d}{dt}[\theta_1(a_1,a_2,\theta_1,\theta_2)-\theta_2(a_1,a_2,\theta_1,\theta_2)]=0. \tag{38c}$$

From initial inspection, Eqs. (38a)–(38c) seem unsolvable because they contain four variables (a_1, a_2, θ_1, θ_2). However, as mentioned earlier, the independent treatment of θ_1 and θ_2 in the steady state is not meaningful, but the difference between the two is significant. After introducing the relationship $\theta_1=\hat{\theta}+\theta_2$ into Eqs. (38a)–(38c) and setting a reference value $\overline{\theta}_2$ for θ_2, we can obtain three coupled differential equations as functions of a_1, a_2 and $\hat{\theta}$. These equations are solvable and may take the following form

$$\dot{y}_1=\varepsilon\,\mathrm{Re}[2\Phi_1^{(1)}e^{-i(y_3+\overline{\theta})}]+\varepsilon^2\,\mathrm{Re}[2(\zeta_1^{(1)}-D_1C_1^{(1)})e^{-i(y_3+\overline{\theta})}]+\cdots=0, \tag{39a}$$

$$\dot{y}_2=\varepsilon\,\mathrm{Re}[2\Phi_3^{(1)}e^{-i\overline{\theta}}]+\varepsilon^2\,\mathrm{Re}[2(\zeta_3^{(1)}-D_1C_2^{(1)})e^{-i\overline{\theta}}]+\cdots=0, \tag{39b}$$

$$\dot{y}_3=\varepsilon\left\{\frac{1}{y_1}\mathrm{Im}[2\Phi_1^{(1)}e^{-i(y_3+\overline{\theta}_2)}]-\frac{1}{y_2}\mathrm{Im}[2\Phi_3^{(1)}e^{-i\overline{\theta}_2}]\right\}+\varepsilon^2\left\{\frac{1}{y_1}\mathrm{Im}[2(\zeta_1^{(1)}-D_1C_1^{(1)})e^{-i(y_3+\overline{\theta}_2)}]-\frac{1}{y_2}\mathrm{Im}[2(\zeta_3^{(1)}-D_1C_2^{(1)})e^{-i\overline{\theta}_2}]\right\}+\cdots=0, \tag{39c}$$

where $\Phi_1^{(1)}$, $\Phi_3^{(1)}$, $\zeta_1^{(1)}$ and $\zeta_3^{(1)}$ are functions of y_1, y_2, and y_3. The definition

$$\{y_1,y_2,y_3\}=\{a_1,a_2,\hat{\theta}\} \tag{40}$$

is employed for notation convenience.

The solutions of Eqs. (39a)–(39c) represent the steady state periodic responses of the system, i.e., the limit cycles. Once these solutions are obtained, Lyapunov's indirect method described in Appendix B can be applied to determine the stability of the associated limit cycles. In the case where any of the eigenvalues of the linearized system matrix $\mathbf{A}'$ of Eq. (B.4) has a positive real part, the limit cycle in the steady state is unstable; or else it is stable. The focus of this study is to examine the behavioral characteristics of a full railway vehicle in every possible steady state condition. Hence, the application of Lyapunov's indirect method could be an effective way to determine 'the stability of the limit cycles' corresponding to the respective steady state solutions.

6. Results and discussions

6.1. Dynamic simulation for attaining the asymptotic solutions at the hunting speed

Prior to performing any sophisticated bifurcation analysis on the full railway vehicle system, a series of numerical simulations were done to support the validity of such approaches. For these simulations, the parameters listed in Appendix C were used.

Principal modal coordinates and modulation equations for the first, second, and third approximations were numerically evaluated through direct time integrations using the fourth-order Runge–Kutta method. The state-space responses of the reduced railway vehicle system can be obtained by summing up the modal coordinates multiplied by their corresponding modal vectors, and compared to results obtained from direct numerical integration.

Fig. 3 shows the frequency responses of the first three asymptotic approximations of the lateral displacement of the leading wheelset in the front bogie with the linear and heuristic creep models. For notation brevity, the terminology "lateral displacement" will be used hereafter to represent the "lateral displacement of the leading wheelset in the front bogie", unless mentioned otherwise. In the numerical simulation, the vehicle speed is set to be the hunting speed of the linearized system, which is 377 km/h with the linear creep model and 376 km/h with the heuristic creep model.

As evident in Fig. 3, the response obtained using only the first-order approximation cannot explain the second or higher order resonant frequency components. In contrast, the higher-order approximations can adequately explain such components. Note that the lateral displacement of the railway vehicle is composed of higher resonant frequency components and fundamental frequency components, which are at least 30 dB greater than the higher components and hence dominates the lateral behavior of the vehicle. Although the accuracy of the response improves with the order of approximation, this result show that the response obtained using the second-order approximation can be considered sufficiently accurate to describe the hunting behavior of the vehicle. Thus, the modal coordinates are asymptotically expanded up to the second-order in this study.

Fig. 4 shows the limit cycles of the lateral displacement represented in a phase plane with the linear and heuristic creep models. Since the degree of nonlinearity from the heuristic creep model is larger than the one from the linear creep model, the limit cycle of the former case tends to be more distorted from a perfect circle. However, it can be seen from these figures that for both cases the phase portraits, when using the asymptotic expansion up to the second-order, are in good agreement with those obtained using direct numerical integration.

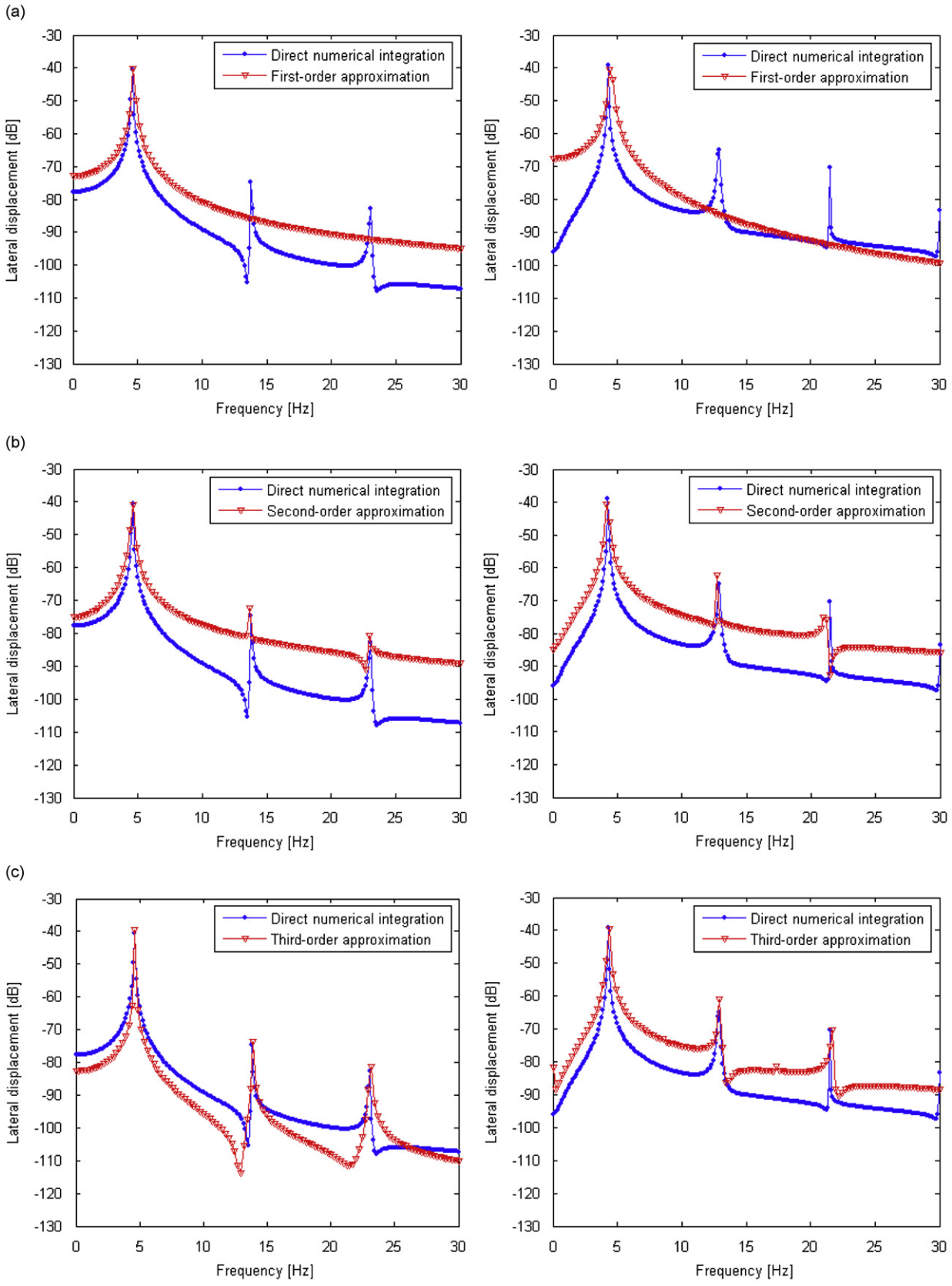

Fig. 3. Frequency responses of the lateral displacement of the leading wheelset in the front bogie with the linear creep model (first column) and the heuristic creep model (second column): (a) the first, (b) the second, and (c) the third asymptotic approximations.

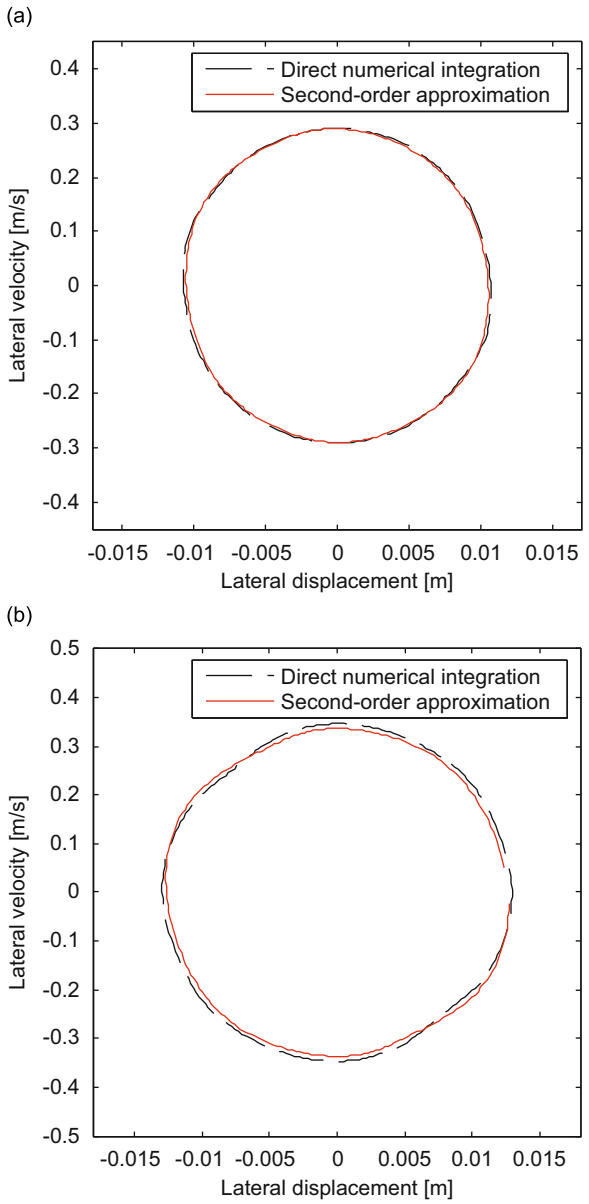

Fig. 4. Phase portraits of the lateral motion of the vehicle model with: (a) the linear creep model and (b) the heuristic creep model.

Table 1
Comparison of the maximum lateral displacements for the first and second approximations.

	Running speed (km/h)	Maximum lateral displacement (m)		
		Numerical integration	First approximation (%)	Second approximation (%)
Cycle I	525.5	1.741×10^{-3}	2.55×10^{-3} (46)[a]	1.784×10^{-3} (2.4)
Cycle II		1.06×10^{-2}	1.062×10^{-2} (0.2)	1.039×10^{-2} (2.0)
Cycle I	550	2.07×10^{-3}	–[b]	2.153×10^{-3} (4.0)
Cycle II		1.08×10^{-2}	1.07×10^{-2} (0.5)	1.062×10^{-2} (0.9)

[a] Percent error of the maximum lateral displacement of the approximations with respect to that of the numerical simulation.
[b] Could not be obtained using the first approximation.

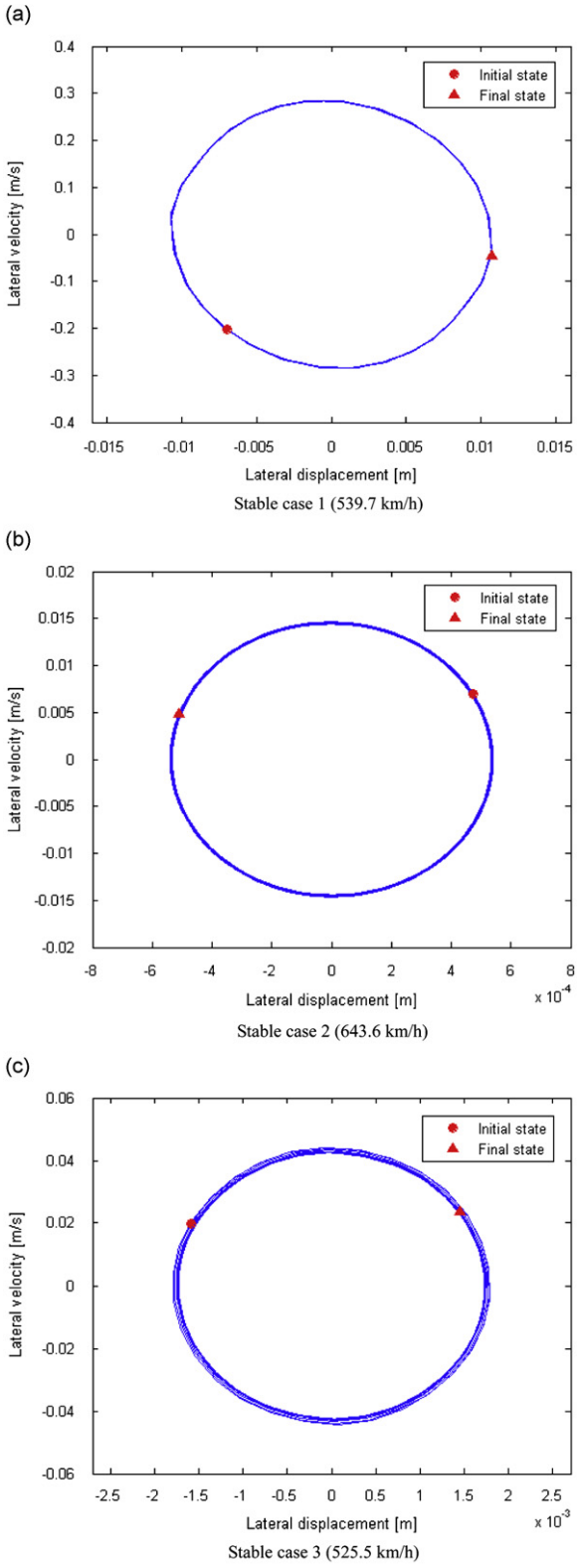

Fig. 5. Phase portraits for the lateral displacement with three stable initial conditions (cases 1, 2, and 3 correspond to the stable points a, b, and c in Fig. 10, respectively).

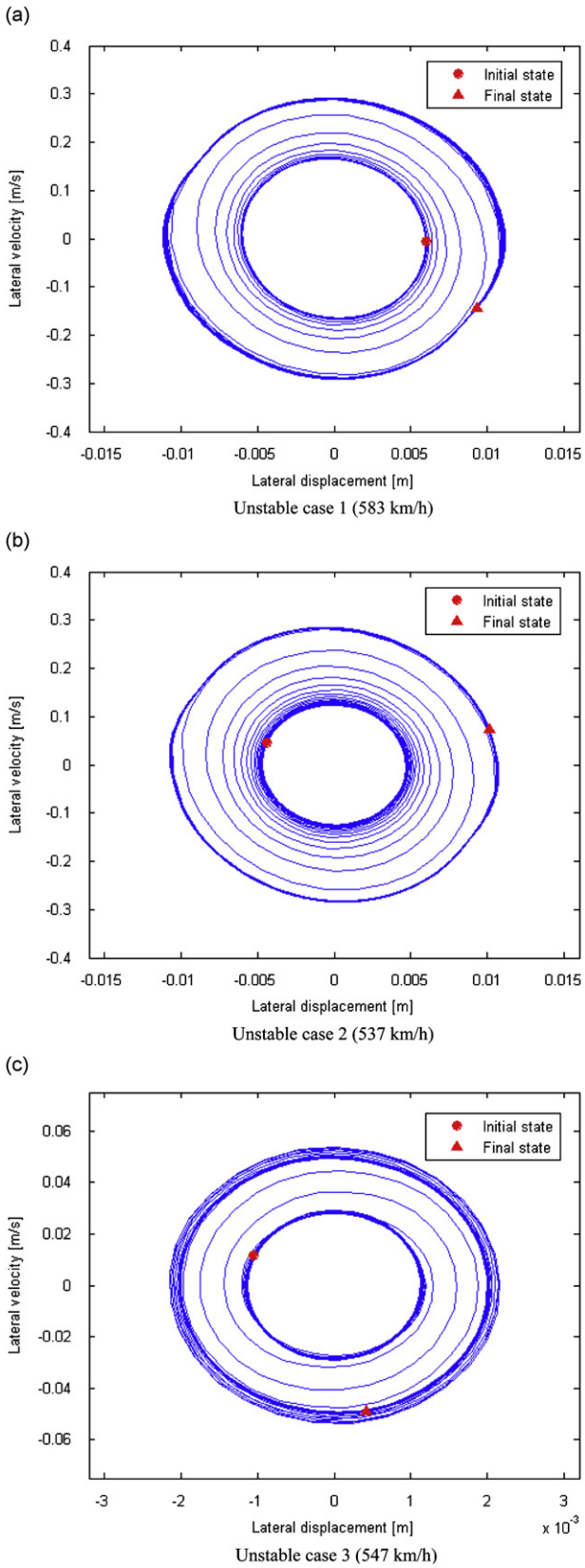

Fig. 6. Phase portraits for the lateral displacement with three unstable initial conditions (cases 1, 2, and 3 correspond to the stable points d, e, and f in Fig. 10, respectively).

6.2. Effectiveness of the solutions for asymptotic approximation

To validate the effectiveness of the solutions obtained from asymptotic approximation, numerical simulations are performed using Eq. (9). In these simulations, heuristic creep theory is applied using the parameters listed in Appendix C. The values of damping constants C_{pz}, C_{sx}, C_{sy}, and C_{sz} are enclosed in parentheses. Several limit cycles, used as initial states in the simulations, and their corresponding stabilities are computed. The vehicle's initial conditions (and running speed) are set to correspond to three stable cases and three unstable cases.

The amplitudes of the stable limit cycles obtained from direct integration and those from the solutions of the first and second approximations using the method of multiple scales are listed and compared in Table 1. Running speeds of 525.5 and 550 km/h were used for both methods. For the first approximation, the errors are very large (the maximum percent error is about 46 percent) and some limit cycles are unattainable. For the second approximation, the errors are significantly reduced (the maximum percent error is about 4 percent) and all the limit cycles are obtainable.

Fig. 5 shows the phase portraits obtained using the simulation results for the three stable (attractive) initial states evaluated by the second-order approximation. In these figures, the symbol of a solid circle denotes the initial state and a solid triangle represents the final state in the time interval of computation. In the case where the initial state is stable, the simulation results show ellipses in the phase plane. It can be seen on Fig. 4(c) that the final trajectory is slightly diminished in size when compared to the initial state.

Fig. 6 shows the phase portraits obtained using the simulation results for the three unstable (non-attractive) initial states. As evident from these figures, the trajectory starting from the unstable limit cycle slowly diverges from the cycle and converges to another attractive limit cycle. The stability results shown in Figs. 5 and 6 are in good agreement with the stability from the corresponding initial states. Therefore, the second-order approximation can logically be used to perform the bifurcation analysis on the full vehicle system considered in this study.

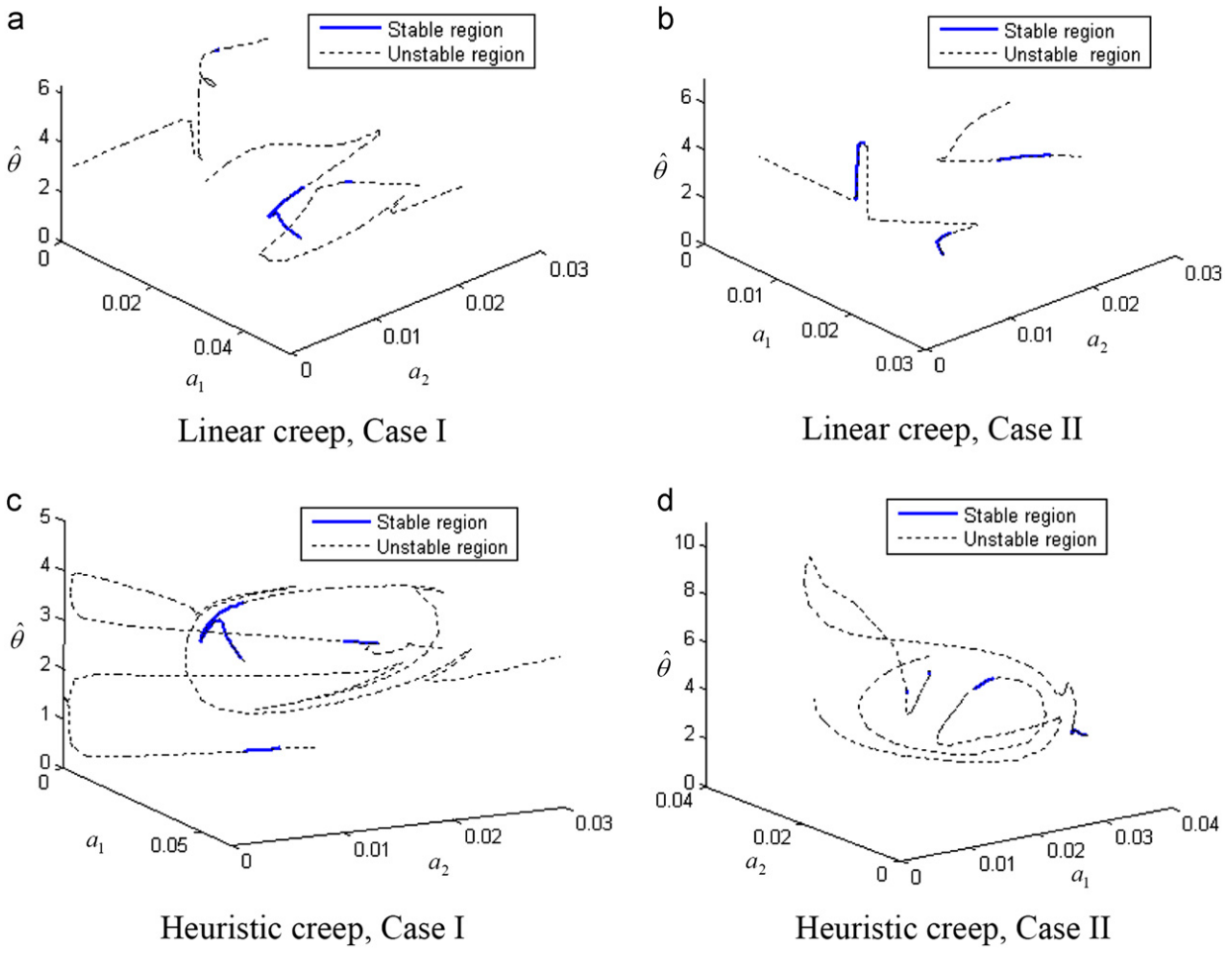

Fig. 7. Steady state solutions for the amplitudes of the modal coordinates and their phase difference.

6.3. Bifurcation analysis

To investigate the bifurcation behavior of the vehicle system, the limit cycles in the vicinity of the linear critical speed are obtained from the response by using the second-order asymptotic approximation and the method of multiple scales. As a first step, the solutions of Eqs. (39a), (39b), and (39c) are computed numerically by using the multivariable Newton–Raphson method [29] to obtain the limit cycle behaviors, i.e., the amplitudes of the modal coordinates and their phase differences at the steady state. Since the focus of this study is to examine the hunting behavior of the railway vehicle model, the bifurcation diagrams for the lateral displacement are obtained. Furthermore, in order to investigate the effects of the hunting speed on the bifurcation behavior, two different set of values for the damping constants C_{pz}, C_{sx}, C_{sy}, and C_{sz} are used in the computation, specifically 15, 200, 30, 80 kNs/m for Case I and 450, 10, 10, 88 kNs/m for Case II. Other parameters and their respective values are listed in Appendix C.

Fig. 7 shows the steady state amplitudes (a_1, a_2) of the associated modal coordinates and their phase difference ($\hat{\theta}$) within a speed range of 250–750 km/h. Each diagram includes at least two branches, each composed of a stable (or unstable) solution region that indicates a stable (or unstable) limit cycle, respectively. At least one stable region is also included for each branch.

The branches obtained from the steady state amplitudes and their phase difference for the system with the heuristic creep model [(c), (d) in Fig. 7] tend to vary widely and are more complicated than those attained with the linear creep model. The heuristic creep model includes nonlinear saturation factors that play a role in confining, within certain physical limits, the creep forces acting between the rail and the wheel contact interfaces. Also, the heuristic creep model tends to produce creep forces that become more insensitive to variations in the states as the saturation factors approach their limits. Thus, it is considered to be more realistic than the linear creep model. This may explain the variance in the behavior of the branches when the heuristic creep model is employed.

Figs. 8 and 9 show the maximum lateral displacement as a function of the vehicle running speed based on the linear and heuristic creep theories, respectively. System parameters for Case I are used. In Fig. 8, point A designates the equilibrium point at the linear critical speed ($\approx$ 377 km/h) from which the branch becomes unstable; it is called the subcritical Hopf bifurcation. A branch bifurcating from the equilibrium solution changes from unstable to stable at point B, which is called a fold or saddle-node bifurcation because the solution changes the stability when it moves around the fold [7]. In nonlinear dynamics, a change in the number of solutions will occasionally occur through such bifurcation(s) from an existing solution under a continuous change in a parameter [7]. The running speed of the vehicle corresponding to this saddle-node bifurcation point is the nonlinear

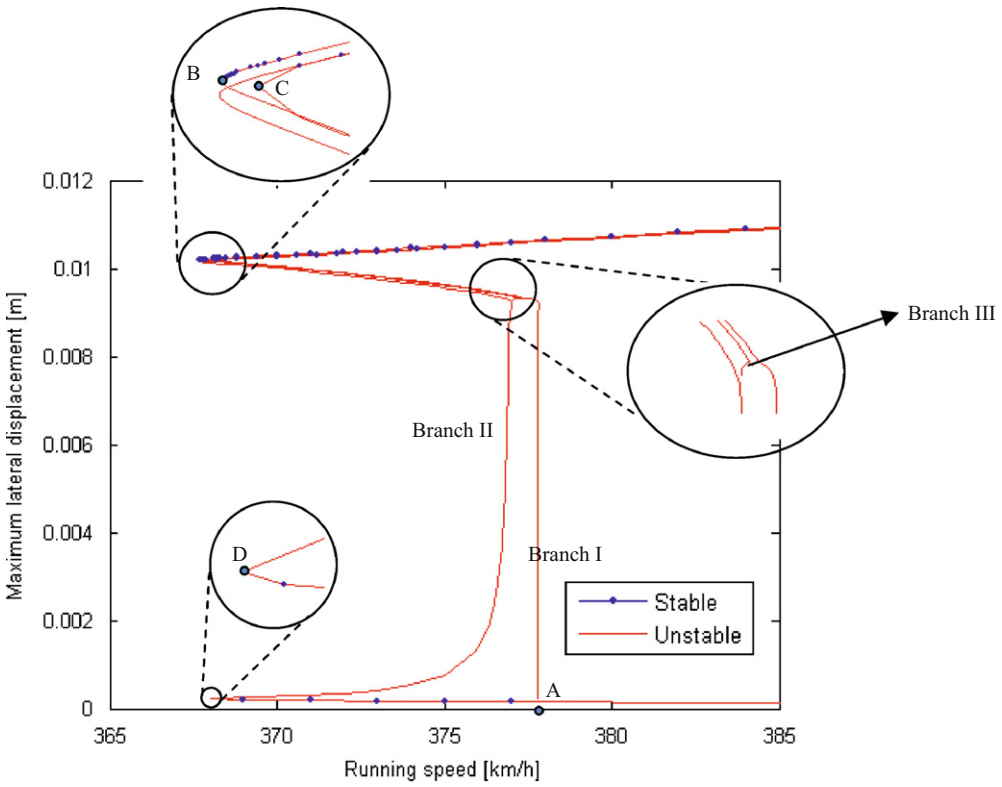

Fig. 8. Bifurcation diagram for the lateral displacement of the vehicle with the linear creep model.

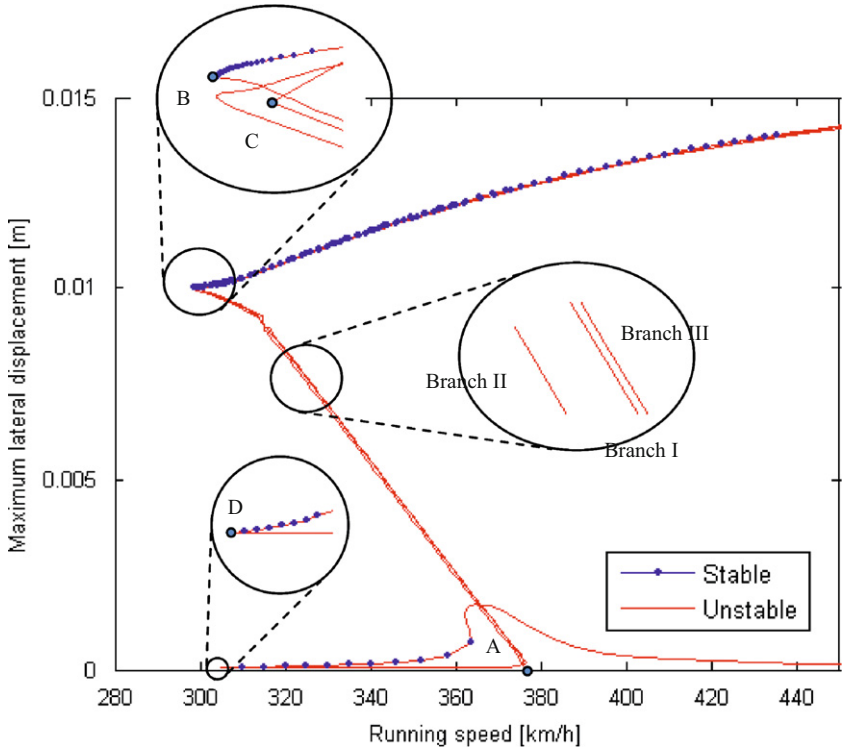

Fig. 9. Bifurcation diagram for the lateral displacement of the vehicle with the heuristic creep model.

critical speed ($\approx$ 367 km/h), which should be given serious attention when designing railway vehicle systems. Note here that the critical speed of this nonlinear system is smaller than that of the linearized system (i.e. the hunting speed).

One bifurcation branch, composed mainly of subcritical Hopf bifurcation and saddle-node bifurcation, is well-known from previous research [19–21]. However, with a dual-bogie system, additional branches exist. These branches bifurcate from a point different from the equilibrium point, from which Branch I in Fig. 8 bifurcates.

One of the branches (Branch II) includes two saddle node bifurcation points and is composed of many separate stable and unstable regions. This branch changes from unstable to stable (or from stable to unstable) at points C and D. The other branch (Branch III) is unstable. The existence of such additional branches means that, unlike a single-bogie vehicle system, there are many stable or unstable coexisting solutions in a dual-bogie vehicle system. More specifically, the number of coexisting limit cycles below the linear critical speed is eight (the maximum number), with three that are stable (or attractive) limit cycles. From this observation, it can be inferred that the vehicle system has multiple stable limit cycles, and each may give the states that stabilize the vehicle over a long period of time.

For the case where heuristic creep theory is applied, the bifurcation diagrams, similar to those of the linear creep model, are composed of three branches: a bifurcation branch (Branch I) that includes the subcritical Hopf bifurcation (point A) and the saddle-node bifurcation (point B), a bifurcation branch (Branch II) that includes two saddle-node bifurcations (points C and D), and an unstable branch (Branch III). These are shown in Fig. 9. Although the linear critical speeds obtained using linear and heuristic creep theories are quite similar (377 and 376 km/h, respectively), the critical speed obtained with the nonlinear creep theory ($\approx$ 295 km/h) is much lower than the critical speed obtained with the linear creep theory ($\approx$ 366 km/h). This is caused by the saturation of creep forces when the nonlinear creep theory is applied.

Fig. 10 shows the bifurcation diagrams for the lateral displacement when we used the system parameters for Case II. Two and three branches are exhibited in these figures for the cases where, respectively, the linear and heuristic creep theories are applied. Unlike the branches depicted in Figs. 8 and 9 for Case I, the branches for Case II exhibit a wider spread.

The shape of bifurcation branches seems to strongly depend on system parameters. The branches obtained using the heuristic creep theory, shown in Fig. 10(b), are spatially more complicated than the branches obtained from the linear creep theory. In addition, approximately twice as many branches are obtained using the heuristic creep model than are obtained using the linear creep model.

The linear critical speeds obtained using the linear creep theory (Fig. 10(a)) and the heuristic creep theory (Fig. 10(b)) are 644 and 641 km/h, respectively, whereas their respective nonlinear critical speeds are 627 and 480 km/h. This trend is similar to the one observed when the parameters for Case I are used.

Note that points a, b, and c in Fig. 10 correspond to the stable initial states of cases 1, 2, and 3 shown in Fig. 5, respectively. Also, points d, e, and f correspond to the unstable states of cases 1, 2, and 3 shown in Fig. 6, respectively.

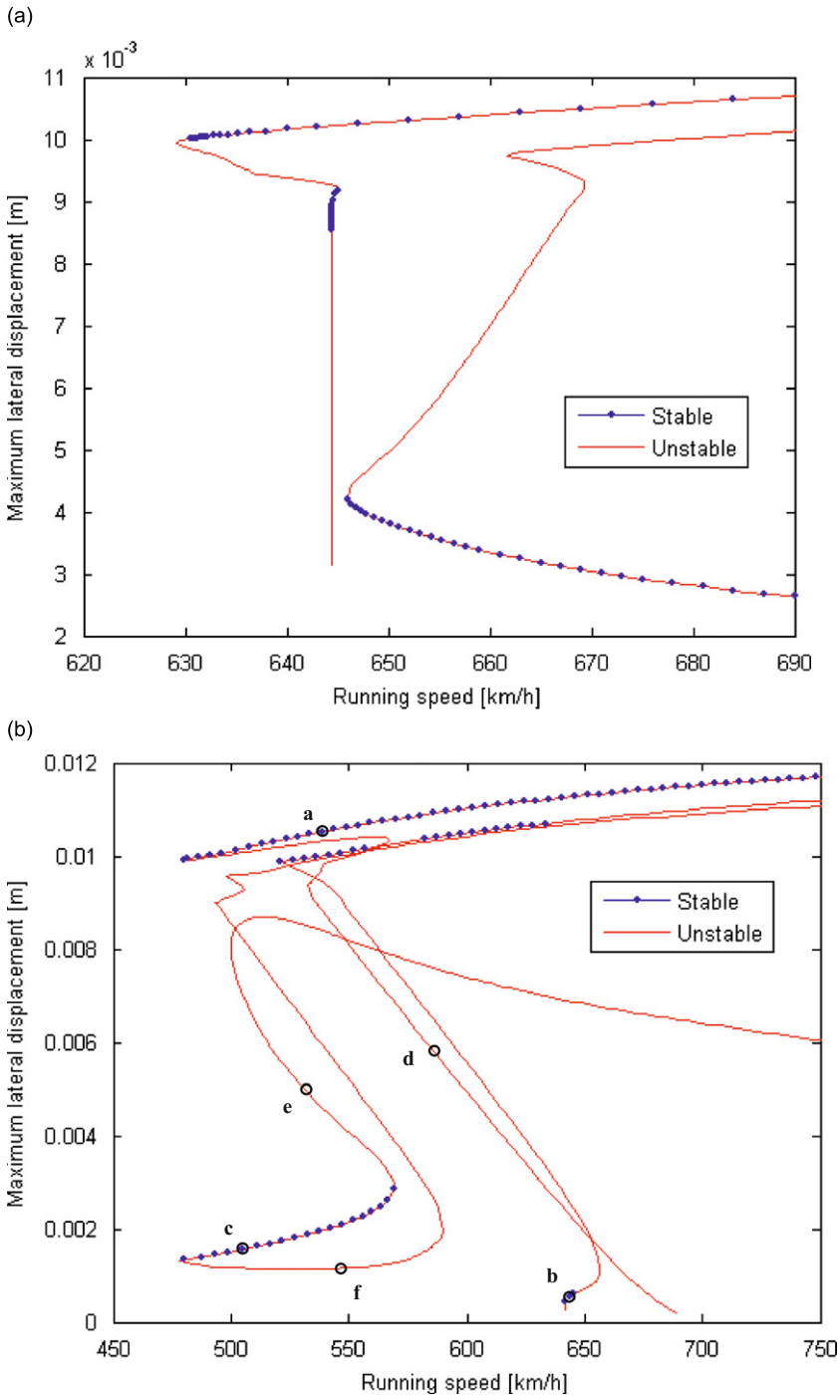

Fig. 10. Bifurcation diagrams for the lateral displacement of the vehicle when using: (a) linear creep theory and (b) heuristic creep theory.

Through a comparison of the results shown in Figs. 5, 6, and 10(b), it can be seen that the stability behavior in the bifurcation diagrams are in good agreement with those obtained from numerical simulations.

7. Conclusions

A bifurcation analysis is performed to examine the nonlinear characteristics of a 31-DOF full railway system that includes a lightly-coupled dual-bogie system. The reduced system equations of the 4 principal eigenmodes (two most

dominant and their corresponding shadow) is adopted, assuming the contribution of the remaining modes is negligible. A scaling parameter is introduced to emulate a system that oscillates with a monofrequency. The modulation equations for the amplitudes and phase difference of the modal coordinates are obtained from these reduced equations through a series of asymptotic approximations and the method of multiple scales.

Numerical simulations are performed to support the effectiveness of the bifurcation analysis. The limit cycles are obtained from the modulation equations at steady state conditions and their stability is determined by Lyapunov's indirect method. These results are compared with those obtained from direct numerical integration. It is shown that at least a second order approximation is needed to obtain reliable results for the vehicle system under consideration.

Using the linear and nonlinear creep theories, bifurcation diagrams are obtained for dual-bogie vehicle systems with different parametric values. It is established that the nonlinear full vehicle system has more limit cycle branches than a single-bogie vehicle system. One branch includes the sub-critical Hopf bifurcation and the saddle node bifurcation, while the other branches include the saddle node bifurcation or show unstable behavior. These multiple limit cycle branches indicate the presence of coexisting solutions at a fixed speed. The configuration and distribution of limit cycle branches seem to strongly depend on system parameters. Using the nonlinear creep model, the difference between the nonlinear and linear critical speeds for the vehicle system appeared to be larger than the difference obtained using the linear creep model.

Acknowledgment

This research was supported by the Chung-Ang University Research Grants in 2009.

Appendix A

A.1. Suspension forces and moments for the vehicle body

$$\begin{aligned}F_{syc} = {} & -2K_{sy}(y_c-y_{t1})-2C_{sy}(\dot{y}_c-\dot{y}_{t1})-2K_{sy}((h-h_G-h_0)\phi_c+h_0\phi_{t1})-2C_{sy}((h-h_G-h_0)\dot{\phi}_c+h_0\dot{\phi}_{t1})\\ & -2K_{sy}(y_c-y_{t2})-2C_{sy}(\dot{y}_c-\dot{y}_{t2})-2K_{sy}((h-h_G-h_0)\phi_c+h_0\phi_{t2})-2C_{sy}((h-h_G-h_0)\dot{\phi}_c+h_0\dot{\phi}_{t2}),\end{aligned} \tag{A.1}$$

$$F_{szc} = -2K_{sz}(z_c-z_{t1})-2C_{sz}(\dot{z}_c-\dot{z}_{t1})-2K_{sz}(z_c-z_{t2})-2C_{sz}(\dot{z}_c-\dot{z}_{t2}), \tag{A.2}$$

$$\begin{aligned}M_{sxc} = {} & (h-h_G-h_0)(-2K_{sy}(y_c-y_{t1})-2C_{sy}(\dot{y}_c-\dot{y}_{t1}))-2((h-h_G-h_0)\phi_c+h_0\phi_{t1})-2C_{sy}((h-h_G-h_0)\dot{\phi}_c+h_0\dot{\phi}_{t1})-2K_{sy}(y_c-y_{t2})\\ & -2C_{sy}(\dot{y}_c-\dot{y}_{t2})-2K_{sy}((h-h_G-h_0)\phi_c+h_0\phi_{t2})-2C_{sy}((h-h_G-h_0)\dot{\phi}_c+h_0\dot{\phi}_{t2})+b_{c3}(-2K_{sz}b_{c3}(\phi_c-\phi_{t1})-2K_{sz}b_{c3}(\phi_c-\phi_{t2}))\\ & +b_{c4}(-2C_{sz}b_{c4}(\dot{\phi}_c-\dot{\phi}_{t1})-2C_{sz}b_{c4}(\dot{\phi}_c-\dot{\phi}_{t2})),\end{aligned} \tag{A.3}$$

$$\begin{aligned}M_{syc} = {} & L_c(2K_{sz}(z_c-z_{t1})-4K_{sz}L_c\gamma_c+2C_{sz}(\dot{z}_c-\dot{z}_{t1})-4C_{sz}L_c\dot{\gamma}_c-2K_{sz}(z_c-z_{t2})-2C_{sz}(\dot{z}_c-\dot{z}_{t2})+(h-h_G-h_0)(-2K_{sx}((h-h_G-h_0)\gamma_c+h_0\gamma_{t1})\\ & -2C_{sx}((h-h_G-h_0)\dot{\gamma}_c+h_0\dot{\gamma}_{t1})-2K_{sx}((h-h_G-h_0)\gamma_c+h_0\gamma_{t2})-2C_{sx}((h-h_G-h_0)\dot{\gamma}_c+h_0\dot{\gamma}_{t2})),\end{aligned} \tag{A.4}$$

$$\begin{aligned}M_{szc} = {} & b_{c1}(-2K_{sx}b_{c1}(\psi_c-\psi_{t1})-2K_{sx}b_{c1}(\psi_c-\psi_{t2}))+2b_{c2}(-2C_{sx}b_{c2}(\dot{\psi}_c-\dot{\psi}_{t1})-2C_{sx}b_{c2}(\dot{\psi}_c-\dot{\psi}_{t2}))\\ & +L_c(-2K_{sx}(y_c-y_{t1})-2C_{sy}(\dot{y}_c-\dot{y}_{t1})-4K_{sy}L_c\psi_c-4C_{sy}L_c\dot{\psi}_c-2K_{sy}((h-h_G-h_0)\phi_c+h_0\phi_{t1})-2C_{sy}((h-h_G-h_0)\dot{\phi}_c+h_0\dot{\phi}_{t1})\\ & +2K_{sy}(y_c-y_{t2})+2C_{sy}(\dot{y}_c-\dot{y}_{t2})+2K_{sy}((h-h_G-h_0)\phi_c+h_0\phi_{t2})+2C_{sy}((h-h_G-h_0)\dot{\phi}_c+h_0\dot{\phi}_{t2})).\end{aligned} \tag{A.5}$$

A.2. Suspension forces and moments for the bogie frames

$$\begin{aligned}F_{syti} = {} & 2K_{sy}(y_c-y_{ti})+2C_{sy}(\dot{y}_c-\dot{y}_{ti})-2(-1)^{i}K_{sy}L_c\psi_c-2(-1)^{i}C_{sy}L_c\dot{\psi}_c+2K_{sy}((h-h_G-h_0)\phi_c+h_0\phi_{ti})\\ & +2C_{sy}((h-h_G-h_0)\dot{\phi}_c+h_0\dot{\phi}_{ti})-2K_{py}(y_{ti}-y_{wi1})-2K_{py}(L_{t1}\psi_{ti}-L_w\psi_{wi1})-4C_{py}h_G\dot{\phi}_{ti}-2K_{py}(y_{ti}-y_{wi2})\\ & +2K_{py}(L_{t1}\psi_{ti}-L_w\psi_{wi2})-2C_{py}(\dot{y}_{ti}-\dot{y}_{wi2})+2C_{py}(L_{t2}\dot{\psi}_{t2}-L_w\dot{\psi}_{wi2}),\end{aligned} \tag{A.6}$$

$$F_{szti} = 2K_{sz}(z_c-z_{ti})-2(-1)^{i}K_{sz}L_c\gamma_c+2C_{sz}(\dot{z}_c-\dot{z}_{ti})-2(-1)^{i}C_{sz}L_c\dot{\gamma}_c-2K_{pz}(z_{ti}-z_{wi1})-2C_{pz}(\dot{z}_{ti}-\dot{z}_{wi1})-2K_{pz}(z_{ti}-z_{wi2})-2C_{pz}(\dot{z}_{ti}-\dot{z}_{wi2}), \tag{A.7}$$

$$\begin{aligned}M_{sxti} = {} & 2b_{c3}^2K_{sz}(\phi_c-\phi_{ti})+2b_{c4}^2C_{sz}(\dot{\phi}_c-\dot{\phi}_{ti})+h_0(-2K_{sy}(y_c-y_{ti})-2C_{sy}(\dot{y}_c-\dot{y}_{ti}))-2(-1)^{i}K_{sy}L_c\psi_c-2(-1)^{i}C_{sy}L_c\dot{\psi}_c-2K_{sy}((h-h_G-h_0)\phi_c\\ & +h_0\phi_{ti}-2C_{sy}((h-h_G-h_0)\dot{\phi}_c+h_0\dot{\phi}_{ti}))+b_{t3}(-2K_{pz}b_{t3}(\phi_{ti}-\phi_{wi1})-2K_{pz}b_{t3}(\phi_{ti}-\phi_{wi2}))+b_{t4}(-2C_{pz}b_{t4}(\dot{\phi}_{ti}-\dot{\phi}_{wi1})\\ & -2C_{pz}b_{t4}(\dot{\phi}_{ti}-\dot{\phi}_{wi2}))+h_G(-2K_{py}(y_{t1}-y_{wi1})-2K_{py}(L_1\psi_{ti}+L_w\psi_{wi1})-4K_{py}h_G\phi_{ti}-2C_{py}(\dot{y}_{ti}-\dot{y}_{wi1})-2C_{py}(L_{t2}\dot{\psi}_{ti}-L_w\dot{\psi}_{wi1})\\ & -4C_{py}h_G\dot{\phi}_{ti}-2K_{py}(y_{ti}-y_{wi2})+2K_{py}(L_{ti}\psi_{ti}+L_w\psi_{wi2})-2C_{py}(\dot{y}_{ti}-\dot{y}_{wi2})+2C_{py}(L_{t2}\dot{\psi}_{ti}-L_w\dot{\psi}_{wi2})),\end{aligned} \tag{A.8}$$

$$\begin{aligned}M_{syti} = {} & h_0(-2K_{sx}((h-h_G-h_0)\gamma_c+h_0\gamma_{ti})-2C_{sx}((h-h_G-h_0)\dot{\gamma}_c+h_0\dot{\gamma}_{ti}))+h_G(-4K_{px}h_G\gamma_{ti}-4C_{px}h_G\dot{\gamma}_{ti})+L_G(2K_{px}(z_{ti}-z_{wi1})-4K_{pz}L_G\gamma_{ti}\\ & +2C_{pz}(\dot{z}_{ti}-\dot{z}_{wi1})-4C_{pz}L_G\dot{\gamma}_{ti}-2K_{pz}(z_{ti}-z_{wi2})-2C_{pz}(\dot{z}_{ti}-\dot{z}_{wi2})),\end{aligned} \tag{A.9}$$

$$\begin{aligned}M_{szti} = {} & 2b_{c1}^2K_{sx}(\psi_c-\psi_{ti})+2b_{c2}^2C_{sx}(\dot{\psi}_c-\dot{\psi}_{t2})+b_{t1}(-2K_{px}b_{t1}(\psi_{ti}-\psi_{wi1})-2K_{px}b_{t1}(\psi_{ti}-\psi_{wi2}))\\ & +b_{t2}(-2C_{px}b_{t2}(\dot{\psi}_{ti}-\dot{\psi}_{wi1})-2C_{px}b_{t2}(\dot{\psi}_{ti}-\dot{\psi}_{wi2}))+L_{t1}(-2K_{py}(y_{ti}-y_{wi1})-2K_{py}(L_{t1}\psi_{ti}\end{aligned}$$

$$+L_w\psi_{wi1})+2K_{py}(y_{ti}-y_{wi2})-2K_{py}(L_{t1}\psi_{ti}+L_w\psi_{wi2}))+L_{t2}(-2C_{py}(\dot{y}_{ti}-\dot{y}_{wi1})-2C_{py}(L_{t2}\dot{\psi}_{ti}-L_w\dot{\psi}_{wi1}))$$
$$+2C_{py}(\dot{y}_{ti}-\dot{y}_{wi2})-2C_{py}(L_{t2}\dot{\psi}_{ti}-L_w\dot{\psi}_{wi2}). \quad (A.10)$$

A.3. Suspension forces and moments for the wheelsets

$$F_{swyij}=-2K_{py}y_{wij}-2C_{py}\dot{y}_{wij}+2K_{py}y_{ti}+2C_{py}\dot{y}_{ti}-2(-1)^jK_{py}L_{t1}\psi_{ti}-2(-1)^jC_{py}L_{t2}\dot{\psi}_{ti}+2K_{py}h_G\phi_{ti}+2C_{py}h_G\dot{\phi}_{ti}, \quad (A.11)$$

$$F_{szwij}=2K_{pz}z_{ti}+2C_{pz}\dot{z}_{ti}-2K_{pz}z_{wij}-2C_{pz}\dot{z}_{wij}, \quad (A.12)$$

$$M_{szwij}=2K_{px}b_{t1}^2\psi_{ti}-2K_{px}b_{t1}^2\psi_{wij}+2C_{px}b_{t2}^2\dot{\psi}_{ti}-2C_{px}b_{t2}^2\dot{\psi}_{wij}, \quad (A.13)$$

$$M_{sxij}=-2K_{pz}b_{t1}^2\phi_{wij}-2C_{pz}b_{t2}^2\dot{\phi}_{wij}+2K_{pz}b_{t1}^2\phi_{ti}+2C_{pz}b_{t2}^2\dot{\phi}_{ti}. \quad (A.14)$$

A.4. Flange contact forces

$$F_{tij}=\begin{cases}K_{ry}(y_{wij}-\delta) & y_{wij}>\delta,\\ 0 & -\delta\le y_{wij}\le\delta,\\ K_{ry}(y_{wij}+\delta) & y_{wij}<-\delta,\end{cases} \quad (A.15)$$

A.5. Linear creep forces and moments

$$F_{Lxij}=F_{Lxij}^*-F_{Lyij}^*\psi_{wij}, \quad (A.16)$$

$$F_{Lyij}=F_{Lxij}^*\psi_{wij}+F_{Lyij}^*, \quad (A.17)$$

$$F_{Lzij}=F_{Lyij}^*(\delta_L+\phi_{wij}), \quad (A.18)$$

$$M_{Lxij}=M_{Lzij}^*(\delta_L+\phi_{wij})\psi_{wij}, \quad (A.19)$$

$$M_{Lzij}=M_{Lzij}^*, \quad (A.20)$$

$$F_{Rxij}=F_{Rxij}^*-F_{Ryij}^*\psi_{wij}, \quad (A.21)$$

$$F_{Ryij}=F_{Rxij}^*\psi_{wij}+F_{Ryij}^*, \quad (A.22)$$

$$F_{Rzij}=-F_{Ryij}^*(\delta_R-\phi_{wij}), \quad (A.23)$$

$$M_{Rxij}=-M_{Rzij}^*(\delta_R-\phi_{wij})\psi_{wij}, \quad (A.24)$$

$$M_{Rzij}=M_{Rzij}^*, \quad (A.25)$$

A.6. Creep forces and moments given by Kalker's linear theory

$$F_{Lxij}^*=-\frac{f_{33}}{V}\left\{V\left(1+\frac{a}{R_y}-\frac{r_L}{r_0}\right)-a\dot{\psi}_{wij}\right\}, \quad (A.26)$$

$$F_{Lyij}^*=-\frac{f_{11}}{V}(\dot{y}_j+r_L\dot{\phi}_{wij}-V\psi_{wij})-\frac{f_{12}}{V}\left(\dot{\psi}_{wij}-\frac{V}{R_y}-\frac{V}{r_0}\delta_L\right), \quad (A.27)$$

$$M_{Lzij}^*=\frac{f_{12}}{V}(\dot{y}_{wij}+r_L\dot{\phi}_{wij}-V\psi_{wij})-\frac{f_{22}}{V}\left(\dot{\psi}_{wij}-\frac{V}{R_y}-\frac{V}{r_0}\delta_L\right), \quad (A.28)$$

$$F_{Rxij}^*=-\frac{f_{33}}{V}\left\{V\left(1-\frac{a}{R_y}-\frac{r_R}{r_0}\right)+a\dot{\psi}_{wij}\right\}, \quad (A.29)$$

$$F_{Ryij}^*=-\frac{f_{11}}{V}(\dot{y}_{wij}+r_R\dot{\phi}_{wij}-V\psi_{wij})-\frac{f_{12}}{V}\left(\dot{\psi}_{wij}-\frac{V}{R_y}+\frac{V}{r_0}\delta_R\right), \quad (A.30)$$

$$M^*_{Rzij} = \frac{f_{12}}{V}(\dot{y}_{wij} + r_R\dot{\phi}_{wij} - V\psi_{wij}) - \frac{f_{22}}{V}\left(\dot{\psi}_{wij} - \frac{V}{R_y} + \frac{V}{r_0}\delta_R\right). \tag{A.31}$$

A.7. Saturation constants

$$\alpha_{ij} = \begin{cases} \dfrac{1}{\beta_{ij}}\left(\beta_{ij} - \dfrac{1}{3}\beta_{ij}^2 + \dfrac{1}{27}\beta_{ij}^3\right) & \text{for } \beta_{ij} \le 3, \\ \dfrac{1}{\beta_{ij}} & \text{for } \beta_{ij} \ge 3, \end{cases} \tag{A.32}$$

$$\beta_{ij} = \frac{\beta_{Rij} + \beta_{Lij}}{2} \text{ and } \beta_{pij} = \frac{\sqrt{(F^*_{pxij})^2 + (F^*_{pyij})^2}}{\mu\sqrt{(N_{pyij})^2 + (N_{pzij})^2}}, p = L,R, \tag{A.33}$$

$$N_{pzij} = -K_{rz}(z_{wij} - \lambda y_{wij} + a\phi_{wij}), p = L,R, \tag{A.34}$$

$$N_{pyij} = -N_{pzij}\tan(\delta_p + \phi_{wij}) \approx -N_{pzij}(\delta_p + \phi_{wij}), p = L,R. \tag{A.35}$$

A.8. Components of contact position vector

$$R_{Rxij} = a\psi_{wij}, \tag{A.36}$$

$$R_{Ryij} = -a + r_R\phi_{wij}, \tag{A.37}$$

$$R_{Rzij} = -a\phi_{wij} - r_R, \tag{A.38}$$

$$R_{Lxij} = -a\psi_{wij}, \tag{A.39}$$

$$R_{Lyij} = a + r_L\phi_{wij}, \tag{A.40}$$

$$R_{Lzij} = a\phi_{wij} - r_L. \tag{A.41}$$

Appendix B. Lyapunov's indirect method

Differential equations (39a)–(39c) can be expressed in a more convenient vector form as

$$\dot{\mathbf{y}}(t) = \mathbf{F}[\mathbf{y}(t)], \tag{B.1}$$

where $\mathbf{y}(t)$ denotes a three-dimensional vector composed of y_1, y_2 and y_3, and $\mathbf{F}[\mathbf{y}(t)]$ is the corresponding three-dimensional nonlinear vector function composed of the right-hand side of Eqs. (39a)–(39c). The solution of Eq. (B.1) can be represented by the steady state solution $\mathbf{y}_s$ superposed by the perturbed solution $\tilde{\mathbf{y}}(t)$, i.e.,

$$\mathbf{y}(t) = \mathbf{y}_s + \tilde{\mathbf{y}}(t). \tag{B.2}$$

Substituting Eq. (B.2) into (B.1), expanding the right-hand side of the resulting equation in a Taylor series for $\mathbf{y}_s$, and ignoring the higher order terms, the linearized equation of Eq. (B.1) can be obtained in the form

$$\dot{\tilde{\mathbf{y}}}(t) = \mathbf{A}'\tilde{\mathbf{y}}(t) + \mathbf{f}[\tilde{\mathbf{y}}(t)], \tag{B.3}$$

where $\mathbf{f}[\tilde{\mathbf{y}}(t)]$ is the nonlinear forcing term and

$$\mathbf{A}' = \left[\frac{\partial\mathbf{F}}{\partial\mathbf{y}}\right]_{\mathbf{y}=\mathbf{y}_s}. \tag{B.4}$$

The stability of the system in the steady state can be inferred from the eigensolutions obtained from the linearized system matrix $\mathbf{A}'$.

Appendix C. System parameters and their numerical values [5,18,20,21,26,30]

Parameters	Values
Vehicle body, bogie frame, and wheelset masses (kg)	m_c=34,000, m_t=3,000, m_w=1,400
Roll, pitch, and yaw moments of inertia of the vehicle body (kg m^2)	I_{cx}=75.06 × 10^3, I_{cy}, I_{cz}=2.086 × 10^6
Roll, pitch, and yaw moments of inertia of the bogie frame (kg m^2)	I_{tx}=2,260, I_{ty}=2,710, I_{tz}=3,160
Roll, pitch, and yaw moments of inertia of the wheelset (kg m^2)	I_{wx}=915, I_{wy}=140, I_{wz}=915

Primary longitudinal, lateral, and vertical stiffnesses (kN/m)	K_{px}=10,000, K_{py}=5,000, K_{pz}=750
Secondary longitudinal, lateral, and vertical stiffnesses (kN/m)	K_{sx}=150, K_{sy}=150, K_{sz}=400
Primary longitudinal, lateral, and vertical damping coefficients (kNs/m)	C_{px}=12, C_{py}=12, C_{pz}=15 (450)
Secondary longitudinal, lateral, and vertical damping coefficients (kNs/m)	C_{sx}=200 (10), C_{sy}=30 (10), C_{sz}=80 (88)
Vertical and lateral rail stiffnesses (kN/m)	$K_{rz}=62\times10^6$, $K_{ry}=16.17\times10^6$
Radius of the curved track (m)	$R_y=\infty$
Cant angle (rad)	ϕ_{se}=0.0873
Friction coefficient	μ=0.2
Acceleration due to gravity (m/s^2)	g=9.81
Wheel conicity	λ=0.05
Flange clearance (m)	δ=0.00923
Lateral creep coefficient (N)	$f_{11}=10.2\times10^6$
Lateral/spin creep coefficient (N m^2)	f_{12}=3120
Spin creep coefficient (N)	f_{22}=16
Longitudinal creep coefficient (N)	$f_{33}=15\times10^6$
Half of the track gauge (m)	a=0.7465
Wheel radius (m)	r_0=0.4575
Half of the secondary longitudinal and vertical spring arms (m)	b_{c1}, b_{c3}=1.21
Half of the secondary longitudinal and vertical damper arms (m)	b_{c2}, b_{c4}=1.21
Half of the primary longitudinal and vertical spring arms (m)	b_{t1}, b_{t3}=0.978
Half of the primary longitudinal and vertical damper arms (m)	b_{t2}, b_{t4}=0.978
Half of the primary lateral spring and damper arms (m)	L_{t1}, L_{t2}=1.2
Distance between the vehicle body and the bogie frame mass centers (m)	L_c=9
Height of the vehicle body mass center above the wheelset mass center (m)	h=1.4
Height of the secondary suspension above the bogie frame mass center (m)	h_0=0.03
Height of the bogie mass center above the wheelset mass center (m)	h_G=0.44

References

[1] A.K.W. Ahmed, S. Sankar, Lateral stability behavior of railway freight car system with elasto-damper coupled wheelset: part 1—Wheelset model, *Transactions of the ASME: Journal of Mechanisms, Transmissions, and Automation in Design* 109 (1987) 493–499.

[2] A.K.W. Ahmed, S. Sankar, Lateral stability behavior of railway freight car system with elasto-damper coupled wheelset: part 2—Truck model, *Transactions of the ASME: Journal of Mechanisms, Transmissions, and Automation in Design* 109 (1987) 500–507.

[3] T. Hirotsh, K. Terada, M. Hiraishi, S. Yui, Simulation of hunting of rail vehicles (The case using circular wheel profile), *JSME International Journal Series III* 34 (1991) 396–403.

[4] S.Y. Lee, Y.C. Cheng, Hunting stability analysis of high-speed railway vehicle trucks on tangent tracks, *Journal of Sound and Vibration* 282 (2005) 881–898.

[5] S.Y. Lee, Y.C. Cheng, Influences of the vertical and the roll motions of frames on the hunting stability of trucks moving on curved tracks, *Journal of Sound and Vibration* 294 (2006) 441–453.

[6] S.Y. Lee, Y.C. Cheng, Nonlinear analysis on hunting stability for high-speed railway vehicle trucks on curved tracks, *Transactions of the ASME: Journal of Vibration and Acoustics* 127 (2005) 324–332.

[7] H. True, On the theory of nonlinear dynamics and its applications in vehicle systems dynamics, *Vehicle System Dynamics* 31 (1999) 393–421.

[8] H. True, Recent advances in the fundamental understanding of railway vehicle dynamics, *International Journal of Vehicle Design* 40 (2006) 251–264.

[9] R.R. Huilgol, Hopf–Friedrichs bifurcation and the hunting of a railway axle, *Quarterly Journal of Applied Mathematics* 36 (1978) 85–94.

[10] D. Moelle, R. Gasch, Non-linear bogie hunting. *Proceedings of the 7th IAVSD Symposium*, Cambridge, Swets&Zeitlinger, Lisse, 1982, pp. 455–467.

[11] R. Gasch, D. Moelle, K. Knothe, The effect of nonlinearities on the limit cycles of railway vehicles, *Proceedings of the 8th IAVSD Symposium on Vehicle Systems Dynamics in The Dynamics of Vehicles on Roads and Tracks*, Swets&Zeitlinger, Amsterdam/Lisse, 1984, pp. 207–224.

[12] H. True, C. Kaas-Petersen, Perodic, biperiodic and chaotic dynamic behavior of railway vehicles, *Proceedings of the 9th IAVSD Symposium*, 1986, pp. 208–221.

[13] H. True, A method to investigate the nonlinear oscillations of a railway vehicle, *Applied Mechanics Rail Transportation Symposium*, Winter Annual Meeting of ASME, 1988.

[14] H. True, Dynamics of a rolling wheelset, *Applied Mechanics Review* 46 (1993) 438–444.

[15] H. True, Some recent developments in nonlinear railway vehicle dynamics, *1st European Nonlinear Oscillation Conference*, Hamburg, 1993, pp. 129–148.

[16] C. Knudsen, R. Feldberg, A. Jaschinski, Nonlinear dynamic phenomena in the behaviour of a railway wheelset model, *Nonlinear Dynamics* 2 (1991) 389–404.

[17] M. Ahmadian, S. Yang, The effect of system nonlinearities on locomotive bogie hunting stability, *Vehicle System Dynamics* 29 (1998) 365–384.

[18] M. Ahmadian, S. Yang, Hopf bifurcation and hunting behavior of a rail wheelset with flange contact, *Nonlinear Dynamics* 15 (1998) 15–30.

[19] W.-J. Chung, S.-W. Kim, A study on the critical speed of railway vehicles, *Transactions of the Korean Society of Mechanical Engineerings* 24 (2000) 1991–1999.

[20] W.-J. Chung, J.-K. Shim, Influence factors on critical speed hysteresis in railway vehicles, *JSME International Journal Series C* 46 (2003) 278–288.

[21] J. Zeng, P. Wu, Stability analysis of high speed railway vehicles, *JSME International Journal Series C* 47 (2004) 464–470.

[22] A.H. Nayfeh, *Perturbation Methods*, Wiley, New York, 1973.

[23] N.N. Bogoliubov, Y.A. Mitropolsky, *Asymptotic Method in the Theory of Nonlinear Oscillations*, Gordon and Breach, New York, 1961.

[24] C.N. Jensen, M. Golubitsky, H. True, Symmetry, generic bifurcations, and mode interaction in nonlinear railway dynamics, *International Journal of Bifurcation and Chaos* 9 (1999) 1321–1331.

[25] Maple^{TM} User's Manual Release 5, Waterloo Maple Inc., 1997.

[26] Rail Safety and Standards Board. Commentary on permissible track forces for railway vehicles, London, (1995) Technical Commentary GM/RC2513.

[27] R.V. Dukkipati, *Vehicle Dynamics*, CRC Press, Boca Raton, Florida, 2000.

[28] L. Meirovitch, *Elements of Vibration Analysis*, McGraw-Hill, New York, 1986.

[29] H. William, P.F. Brian, A.T. Saul, T.V. William, *Numerical Recipes: The Art of Scientific Computing*, Cambridge University Press, New York, 1986.

[30] X.S. Jin, Z.F. Wen, K.Y. Wang, Z.R. Zhou, Q.Y. Liu, C.H. Li, Three-dimensional train–track model for study of rail corrugation, *Journal of Sound and Vibration* 293 (2006) 830–855.